



ulm university universität
uulm

**Fakultät für
Naturwissenschaften**

Institute of Theoretical
Physics

The Effects of Casimir Interactions in Experiments on Gravitationally-induced Entanglement

Bachelor Thesis

Submitted by:

Jan Bulling
jan.bulling@uni-ulm.de
1109395

Supervised by:

Marit O. E. Steiner, Julen S. Pedernales, Martin B. Plenio

Abstract

Contents

1	Introduction	5
1.1	Feynman's Gedankenexperiment	5
2	A first look	6
2.1	Time evolution under a gravitational potential	10
2.2	Entanglement measures	11
2.3	Issues with the experimental procedure	15
3	Casimir effect	16
3.1	Proximity force approximation	18
3.2	Casimir forces between a conducting plate and a dielectric sphere	20
3.3	Imperfect plate and spheres	22
4	The particle in front of a static shield	24
4.1	Entanglement generation	26
4.2	The optimal setup	29
4.2.1	Orientation	30
4.2.2	Separation, mass and superposition size	35
4.3	Trapping the particle	39
4.4	Discussions	41
5	The consequences of a thermal shield	45
5.1	Thickness and size of the shield	45
5.1.1	Shielding Coulomb-Interactions	46
5.1.2	Shielding Casimir-Interactions	48
5.1.3	Gravitational effects of the shield	49
5.2	Thermal shield vibrations	49
5.2.1	Occupation of the vibrational modes	50
5.3	Discussions on the shield	51
	Bibliography	54
A	TITLE TO BE DONE	58
A.1	Evolution under a gravitational Hamiltonian	58
A.1.1	Using time dependent perturbation theory	58
A.1.2	Using an exact time evolution	59
A.2	Exemplary calculation of E_N	59

Contents

B	Casimir interactions	61
B.1	Polarizability of a dielectric sphere	61
C	The shield and its consequences	63
C.1	Blocking of the shield	63
C.2	Thermal harmonic oscillator	63
D	Calculations	65

1 Introduction

Newton (1687)

Keplers law are inverse square of gravitational force

Maskelyne (1774) Gravitational force of a mountain [1, 2]

Cavendish (1798) Gravitational force via torsion pendulum

1.1 Feynman's Gedankenexperiment

2 A first look

Testing the quantum nature of gravity is no easy task and many proposals seek to detect gravitationally induced entanglement between two masses [3–6] as a form of proof. For all these proposals, gravity is assumed to be mediated by a gravitational field. During a time evolution, this field (like any other external field) can only perform local operations (LO) on the states of the test masses. If gravity is now assumed to behave classically, the propagation between the masses can be described by a classical communication (CC) channel [6, 7]. These LOCC operations however cannot turn an initially unentangled state into an entangled one [8, 9]. It immediately follows, that if one measures the involved masses to be entangled after a mutual gravitational interaction, gravity necessarily has to be quantum in some way. It is important to note, that the opposite of this statement is not true. Measuring unentangled masses does not directly imply the classicality of the gravitational field. This can be seen by considering operations that are non-LOCC and also produce unentangled states like for example the swap operation $|\psi\rangle_A |\phi\rangle_B \rightarrow |\phi\rangle_A |\psi\rangle_B$. This operations obviously can't induce entanglement to initially unentangled states, but requires the perfect exchange of quantum information between the states - which is not possible using classical communication alone. In other words: If one prepares masses initially in a pure product state and measures *any* state which cannot be obtained by LOCC-operations after some final time evolution, it is impossible for gravity to behave classical. One can even go so far and define the term ***quantum gravity*** as any interaction mediated by gravity that cannot be described by LOCC operations alone [7].

A plausible and logical idea for an experiment to test for gravitational induced entanglement is described in this chapter - which is, as a reminder, enough to prove a quantum nature of gravity. It requires the generation of coherent delocalized quantum superpositions of massive objects either as so-called Schrödinger-cat states or squeezed gaussian states [6, 10]. Theses masses are brought close enough together for gravity to have a measurable effect. The distances between different parts of the spatial superpositions must have different distances to the delocalized second mass. As a result - and of course *if gravity behaves quantum* - the states should get entangled. To see this, consider the ideal simplification of a real experimental setup where two bodies with mass m are trapped in an harmonic potential wall (like for example in an optical trap) with frequency ω separated by a distance d . The local Hamiltonian of the system is given by

$$\hat{H}_0 = \sum_{i=1,2} \frac{\hat{p}_i^2}{2m} + \frac{1}{2}m\omega^2\hat{x}_i^2 \quad (2.1)$$

where \hat{x} and \hat{p} are the position and momentum operators satisfying the canonical com-

mutation relation $[\hat{x}_i, \hat{p}_j] = i\hbar\delta_{ij}$. For now, all non-gravitational interactions between the masses have been ignored. In the low energy regime, where the energy transfer during a process is far below the Planck scale $m_p c^2 \sim 10^{19}$ GeV, gravity can be traded as an effective field theory with tools available similar to those for the electromagnetic field and QED [11]. In the non-relativistic limit $v \ll c$, the gravitational interaction can be described by a Newtonian $1/r$ potential acting on the center-of-mass positions, with all classical quantities are replaced by quantum operators [10–12]. Spatial superpositions lead to superpositions of the metric and consequently (in the non-relativistic limit) to a superposed Newtonian potential. The interaction Hamiltonian \hat{H}_G should therefore be describable by

$$\hat{H}_G = -\frac{Gm^2}{|d - \hat{x}_1 + \hat{x}_2|}, \quad (2.2)$$

where $G = 6.6743 \times 10^{-11} \text{ m}^3\text{kg}^{-1}\text{s}^{-2}$ is the gravitational constant. The separation of the masses d is chosen much larger than the extension of the delocalization (in this setup comparable to the position variance of the harmonic oscillator). This condition is realistic given that the biggest spatial delocalization ever achieved in matter wave experiments is in the order of 500 nm [13]. Expanding the Hamiltonian \hat{H}_G for small \hat{x}_i , only the second order term proportional to $(\hat{x}_1 - \hat{x}_2)^2$ can induce entanglement [3]. The zeroth order term is just a overall energy offset, the first order term $\propto (\hat{x}_1 - \hat{x}_2)$ as well as the terms \hat{x}_i^2 result only in a local interaction for each mass separately. The coupling term $-(\hat{x}_1\hat{x}_2 + \hat{x}_2\hat{x}_1) = -2\hat{x}_1\hat{x}_2$ however is very interesting as it couples both oscillators and can thus mediate entanglement. Introducing the ladder operators, the Hamiltonian $\hat{H} = \hat{H}_0 + \hat{H}_G$ can be expressed as [11]:

$$\hat{H} = \sum_{i=1,2} \hbar\omega \hat{a}_i^\dagger \hat{a}_i - \frac{Gm^2}{d^3} \left(\sqrt{\frac{\hbar}{2m\omega}} \right)^2 (\hat{a}_1\hat{a}_2 + \hat{a}_1\hat{a}_2^\dagger + \hat{a}_1^\dagger\hat{a}_2 + \hat{a}_1^\dagger\hat{a}_2^\dagger) \quad (2.3)$$

Applying the *rotating-wave approximation*¹, the terms $\hat{a}_1\hat{a}_2 + \hat{a}_1^\dagger\hat{a}_2^\dagger$ can be dropped. Defining the coupling strength g of the interaction as $g = Gm/\omega d^3$, eq (2.3) can be rewritten as

$$\hat{H} = \sum_{i=1,2} \hbar\omega \hat{a}_i^\dagger \hat{a}_i - \hbar g (\hat{a}_1\hat{a}_2^\dagger + \hat{a}_1^\dagger\hat{a}_2). \quad (2.4)$$

Now, for simplicity and as a simple example, the evolution of the initial Fock state $|\psi(0)\rangle = |10\rangle$ is considered. The gravitational interaction H_G can be treated as a time dependent perturbation and the state evolution is given as (for calculation see appendix A.1.1) [11]

$$|\psi(t=0)\rangle = |10\rangle \xrightarrow{\text{time } t} |\psi(t)\rangle = \mathcal{N} (|10\rangle - i g t |01\rangle + \mathcal{O}(g^2)) \quad (2.5)$$

¹This approximation is known from quantum optics, where all fast oscillating terms in the Hamiltonian can be dropped [7, 11]. In the interaction picture, the ladder operators evolve as $\hat{a}(t) = \hat{a}e^{-i\omega t}$. The terms like $\hat{a}_1(t)\hat{a}_2(t)$ oscillate with frequency 2ω whereas $\hat{a}_1^\dagger(t)\hat{a}_2(t)$ does not oscillate at all. Due to the small coupling, this approximation works very well here.

where \mathcal{N} is an appropriate normalization constant. The evolved state (2.5) is entangled and cannot be reduced into a product of two oscillator Fock states. The entanglement is very small since it is proportional to the gravitational coupling constant gt ². Another interesting result, which underlines the false inference of a classical gravity from observed non-entanglement discussed above can be seen by considering the time evolution of a coherent product state $|\alpha\rangle \otimes |\beta\rangle$ where $\hat{a}|\alpha\rangle = \alpha|\alpha\rangle$. The time evolution is derived in appendix A.1.2 and results in

$$e^{-i\hat{H}t/\hbar}(|\alpha\rangle \otimes |\beta\rangle) = |e^{-i\omega t}(\alpha \cos gt - \beta \sin gt)\rangle \otimes |e^{-i\omega t}(-\alpha \sin gt + \beta \cos gt)\rangle. \quad (2.6)$$

This state is clearly a product state and thus not entangled. But for a time $t_0 = \pi/2g$ the state is effectively the swapped initial state $|\beta\rangle \otimes |\alpha\rangle$ up to a local phase. This swap operation is however, as established earlier, not possible under a LOCC protocol. Thus, even if the resulting state after time evolution under a gravitational interaction is unentangled, we can rule out the classicality of gravity [7, 11]. Gravity must therefore be capable of transmitting quantum information and must be described by a quantum channel.

Experimentally, one requires the ability to generate spatial superpositions of two massive objects with large enough coherence times. Usually the weak gravitational interaction requires coherence times in the order of 100 ms – 10 s for any meaningful and measurable entanglement to build up. The masses should additionally be massive enough for their gravitational effects to be measurable. These requirements impose huge experimental and engineering challenges. To contextualize: The most massive object ever put into a spatial superposition in matter-wave interferometry is in the order of 4×10^{-23} kg [13], whereas the smallest object whose gravitational field has been measured was just below 100 mg [14] - a difference of 19 orders of magnitude. One way to experimentally create such spatial superpositions is giving the masses a spin-1/2 degree of freedom. For example, a nitrogen-vacancy diamonds can be used [6], where the NV site provides the required spin of 1/2. An applied magnetic gradient $\partial_x B$ functions like a “beam splitter” and creates a delocalized state. The extent of this superposition can be calculated and separations in the order of 100 μ m are theoretically achievable [6]. Levitated, trapped particles isolated and shielded in a vacuum can increase environmental isolation by avoiding contact with surrounding noise. The additional forces due to the trapping potential or the gravitational acceleration can be studied in advance. In this thesis, I assume that all required states and superpositions can be prepared experimentally.

The general and idealized problem considered is illustrated in fig. 2.1. Two massive bodies with masses M_A and M_B are initially separated by a center-to-center distance $2L$. The masses are prepared in a coherent delocalized quantum superposition Schrödinger-cat-like state in, for now, a parallel orientation as depicted in fig. 2.1. The extension of the superposition is denoted by Δx and is the same for both masses. It is important to choose the positions of the masses such that the distances between each part of the

²The amount of entanglement can for example be quantified with the later introduced *logarithmic negativity* E_N . For this state, it is given by $E_N(|\psi(t)\rangle\langle\psi(t)|) \simeq 2tg/\log 2 + \mathcal{O}(g^2) \geq 0$.

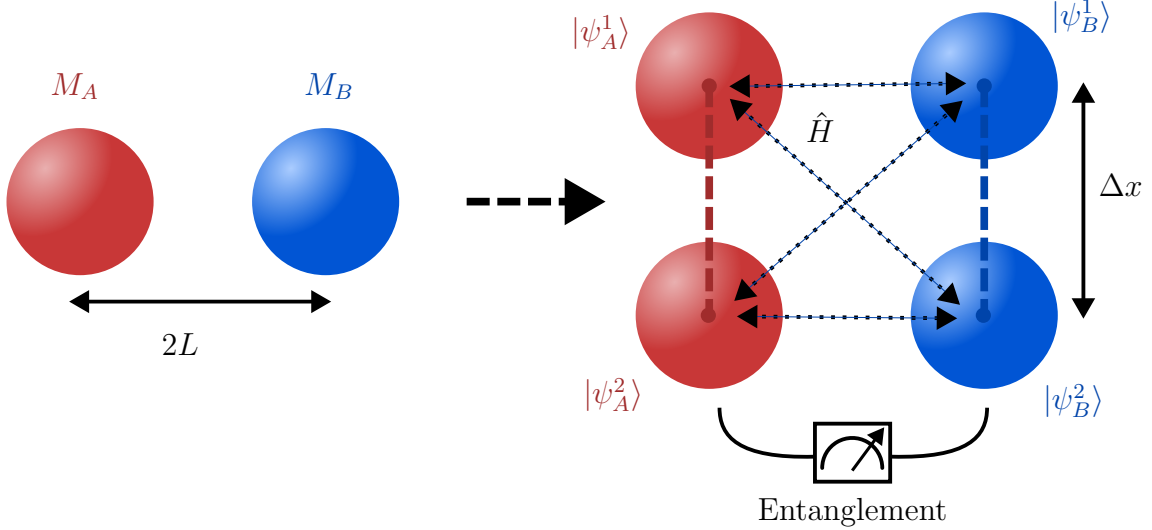


Figure 2.1: Schematic figure of the proposed experiment with two masses prepared in a spatial superposition state. The gravitational interaction \hat{H} induces different phases to each of the superpositions due to the different distances between all masses. This results in measurable entanglement after some time evolution.

delocalized mass A and B are not always identical. Otherwise, all built up phases are the same and no entanglement is observable. With the notation introduced in fig. 2.1, the initial state at $t = 0$ is given by

$$|\psi(t=0)\rangle = \frac{1}{2} (|\psi_A^1\rangle + |\psi_A^2\rangle) \otimes (|\psi_B^1\rangle + |\psi_B^2\rangle). \quad (2.7)$$

The state evolves under a Hamiltonian \hat{H} and after some time the position of each mass is measured and checked for entanglement. For now I assume that all interactions except gravity can be neglected. In reality, electromagnetic forces and Casimir-Polder interactions [15, 16] need to be considered.

As established earlier in this chapter, with some assumptions made, gravitational interaction can generate entanglement. In the time scales of the experiment, the acceleration of the masses due to the mutual gravitational interaction can be neglected³. The Hamiltonian therefore only needs to include the gravitational potential

$$\hat{V} = -\frac{GM_A M_B}{|\hat{D}|} \quad (2.8)$$

where \hat{D} is the distance operator between the masses. It depends on the individual positions \hat{x}_A and \hat{x}_B . During time evolution, the different parts of the superpositions

³Take for example a silica sphere ($\rho = 2648 \text{ kg/m}^3$) with $R = 10^{-5} \text{ m}$ separated by $2L = 4R$. The mutual gravitational acceleration for each sphere is around $a = GM/(2L)^2 = 5 \times 10^{-13} \text{ m/s}^2$ which results for $t \sim 1 \text{ s}$ in a distance traveled of $\sim 10^{-13} \text{ m}$.

built up different local phases. I am interested in calculating, how much entanglement one can expect from this kind of interactions.

2.1 Time evolution under a gravitational potential

Proposition 2.1. *The time evolution under a static and constant Hamiltonian $\hat{H} = \hat{V}(\hat{x}_i) = \text{const.}$ is given by the eigenenergies of the system $\hat{V} |n\rangle = V_n |n\rangle$ proportional to $e^{-iV_n t/\hbar}$.*

Proof. This is a trivial statement. The time evolution is governed by the Schrödinger equation

$$i\hbar \frac{\partial}{\partial t} |\psi(t)\rangle = \hat{H} |\psi(t)\rangle. \quad (2.9)$$

The formal solution of this first order PDE is given by

$$|\psi(t)\rangle = e^{-i\hat{V}t/\hbar} |\psi(t=0)\rangle. \quad (2.10)$$

The constant (hermitian) potential operator can be expressed in the energy-eigenbasis $\{|n\rangle\}$ as $\hat{V} |n\rangle = V_n |n\rangle$. The initial state can be expressed as a superposition in the same eigenstates like $|\psi\rangle = \sum_n c_n |\psi_n\rangle$. Putting both together and using the Taylor expansion of the exponential function, one arrives at the simple form

$$|\psi(t)\rangle = \sum_n e^{-i\hat{V}t/\hbar} |n\rangle \langle n|\psi\rangle = \sum_{n,k} \frac{(-i\hat{V}t/\hbar)^k}{k!} |n\rangle c_n |\psi_n\rangle \quad (2.11)$$

$$= \sum_{n,k} \frac{(-iV_n t/\hbar)^k}{k!} c_n |\psi_n\rangle = \sum_n e^{-iV_n t/\hbar} c_n |\psi_n\rangle \quad (2.12)$$

where in the second to last step $\hat{V}^k |n\rangle = \hat{V}^{k-1} \hat{V} |n\rangle = \hat{V}^{k-1} |n\rangle V_n = \dots = V_n^k |n\rangle$ was used. \square

Using the preceding proposition, the initial state eq. (2.7) can be evolved in time. The potential operator eq. (2.8) acts on every state in the $\{|\psi_A^1\rangle, |\psi_A^2\rangle\} \otimes \{|\psi_B^1\rangle, |\psi_B^2\rangle\}$ basis differently. This is because of the different distances between the states $|\psi_A^i\rangle$ and $|\psi_B^j\rangle$ for different $i, j \in \{1, 2\}$. This results in phases ϕ_{ij} to be built up during time evolution according to proposition 2.1. The state $|\psi(t)\rangle$ after some time evolution is therefore given as

$$|\psi(t)\rangle = \frac{1}{2} \left(e^{i\phi_{11}} |\psi_A^1\rangle |\psi_B^1\rangle + e^{i\phi_{12}} |\psi_A^1\rangle |\psi_B^2\rangle + e^{i\phi_{21}} |\psi_A^2\rangle |\psi_B^1\rangle + e^{i\phi_{22}} |\psi_A^2\rangle |\psi_B^2\rangle \right), \quad (2.13)$$

where the \otimes symbol was omitted. The phases are

$$\phi \equiv \phi_{11} = \phi_{22} = \frac{GM_A M_B}{2\hbar L} t \quad \text{and} \quad \phi_{12} = \phi_{21} = \frac{GM_A M_B}{\hbar \sqrt{4L^2 + (\Delta x)^2}} t. \quad (2.14)$$

Assuming again that the superposition size Δx is much smaller than the distance L between the masses - like before in eq. (2.2) - the phases $\phi_{12} = \phi_{21}$ can be expanded and a global phase ϕ can be factored:

$$\phi_{12} = \phi_{21} \approx \frac{GM_A M_B}{\hbar} \left[\frac{1}{2L} - \frac{(\Delta x)^2}{16L^3} \right] t \equiv \phi - \Delta\phi. \quad (2.15)$$

The state eq. (2.13) can now be expressed in the form

$$|\psi(t)\rangle = e^{i\phi} \frac{1}{\sqrt{2}} \left[|\psi_A^1\rangle \otimes \frac{|\psi_B^1\rangle + e^{-i\Delta\phi} |\psi_B^2\rangle}{\sqrt{2}} + |\psi_A^2\rangle \otimes \frac{e^{-i\Delta\phi} |\psi_B^1\rangle + |\psi_B^2\rangle}{\sqrt{2}} \right], \quad (2.16)$$

where the entanglement dynamics can be directly seen. This state is entangled, if it is not representable as a product state $|\psi\rangle \neq |\psi_A\rangle \otimes |\psi_B\rangle$. That is the case, if the states containing $|\psi_B^i\rangle$ are not both equal to each other (i.e. differ only by a phase) and thus cannot be factored. The system is therefore entangled, if and only if $\Delta\phi \neq k\pi$ with integer $k \in \mathbb{Z}$.

In order to assess in a more quantitative way how entangled the state $|\psi\rangle$ is, a more sophisticated entanglement measure is needed. In the next chapter, the **logarithmic negativity** is motivated and introduced. In the rest of this thesis, I will repeatedly opt for this measure.

2.2 Entanglement measures

Checking whether an arbitrary state ρ is entangled or not is no easy task. In fact, this problem is known to be NP-hard [17]. A state $\rho_{AB} \in \mathcal{H}_A \otimes \mathcal{H}_B$ is called entangled, if it is **non-separable**, that is, it cannot be expressed as a tensor product of two subsystems $\rho_A \in \mathcal{H}_A$ and $\rho_B \in \mathcal{H}_B$. Only for specific cases - like the case of two qubits or qubit-qutrit - a simple sufficient criterion for determining the separability of a general mixed state is known: The positive partial transpose (PPT) criterion states, that if the partial transpose of the density matrix is positive ($\rho^{\Gamma_A} > 0$ ⁴), the state ρ is separable [8, 9]. In other words, if ρ^{Γ_A} has negative eigenvalues, ρ is guaranteed to describe an entangled state. The inverse is true, if and only if the dimension of $\rho_A \otimes \rho_B$ is 2×2 or 3×2 [8] - otherwise, only having non-negative eigenvalues doesn't necessarily result in an unentangled system (such states are called "bound states"). The partial transpose with respect to a subsystem i can be understood in the same way as the partial trace, where the operation (in this case the transform) is performed only on indices corresponding the subsystem ρ_i . To see the necessity of the PPT criterion, consider a separable mixed state ρ , which can be generally expressed as

$$\rho = \sum p_i \rho_A^i \otimes \rho_B^i. \quad (2.17)$$

⁴A matrix is defined as positive ("positive definite"), if all eigenvalues are positive.

The partial transpose is in this case trivial:

$$\rho^{\Gamma_A} = \sum p_i (\rho_A^i)^T \otimes \rho_B^i. \quad (2.18)$$

Since the transpose preserves eigenvalues, the transposed subsystem A is still positive $(\rho_A^i)^T > 0$ and describes again a valid quantum state. It follows, that ρ^{Γ_A} is positive as well. If somehow ρ^{Γ_A} has any negative eigenvalues, this can only mean that the initial state ρ is not separable and cannot be expressed in the form of eq. (2.17) and the necessity of the criterion is shown.

For quantifying entanglement in a more precise way, a mathematical quantity called **entanglement measure** can be used. A good measure should be able to capture the essential features of entanglement. One can axiomatically state what properties such a measure $E(\rho)$ should have [8, 9]:

Normalization An entanglement measure should be a mapping from densities to real positive values between 0 and 1:

$$\rho \rightarrow E(\rho) \in \mathbb{R}^+ \quad (2.19)$$

where usually the maximally entangled state has $E = 1$.

Monotonicity under LOCC E should not increase under local operations and classical communications. This is the most important postulate for an entanglement measure and often cited as the *only* required postulate.

Vanishing on separable states $E(\rho) = 0$ if ρ is separable

Often one finds additional properties useful like *convexity* $E(\sum p_i \rho_i) \leq \sum p_i E(\rho_i)$ or (full) *additivity* $E(\rho \otimes \sigma) = E(\rho) + E(\sigma)$.

A function that satisfies the most important of these conditions is often called an *entanglement monotone*.

The **negativity** \mathcal{N} is such an entanglement monotone [9, 18] that used the PPT criterion to determine if a state is entangled or not. It is defined as

$$\mathcal{N} = \frac{\|\rho^{\Gamma_A}\|_1 - 1}{2} \quad (2.20)$$

where $\|A\|_1 = \text{tr}|A| = \text{tr}\sqrt{A^\dagger A}$ is the trace norm. The negativity however is not additive and a more suitable and widely used entanglement measure is the **logarithmic negativity** [8, 9, 19]

$$E_N(\rho) = \log_2 \|\rho^{\Gamma_A}\|_1. \quad (2.21)$$

The monotonicity of the logarithm implies, that E_N is an entanglement monotone as well. Furthermore, for the calculations it does not matter which subsystem is transposed.

Proposition 2.2. a) The partial transpose w.r.t. subsystem A is equal to the transposed partial transpose w.r.t. subsystem B : $\rho^{\Gamma_A} = (\rho^{\Gamma_B})^T$. b) The trace norms of partially transposed density operators w.r.t. any subsystem are equal: $\|\rho^{\Gamma_A}\|_1 = \|\rho^{\Gamma_B}\|_1$.

Proof. a) A general density matrix ρ can be expressed as

$$\rho = \sum_{i,j,k,l} \rho_{ij,kl} |i\rangle\langle j|_A \otimes |k\rangle\langle l|_B$$

The partial transpose with respect to subsystem B is then defined as

$$\rho^{\Gamma_B} \equiv \sum_{i,j,k,l} \rho_{ij,kl} |i\rangle\langle j|_A \otimes (|k\rangle\langle l|_B)^T = \sum_{i,j,k,l} c_{ij,kl} |i\rangle\langle j|_A \otimes |l\rangle\langle k|_B$$

The complete transpose of this is

$$(\rho^{\Gamma_B})^T = \sum_{i,j,k,l} \rho_{ij,kl} (|i\rangle\langle j|_A)^T \otimes (|l\rangle\langle k|_B)^T = \sum_{i,j,k,l} c_{ij,kl} |j\rangle\langle i|_A \otimes |k\rangle\langle l|_B \equiv \rho^{\Gamma_A}$$

b) Clear by a) and by using lemma 2.1 and the fact that the eigenvalues of a square matrix A and A^T are equal. \square

The logarithmic negativity is very easy to calculate compared to other entanglement measures. It is enough to compute the square root of the eigenvalues of $(\rho^\Gamma)^\dagger \rho^\Gamma$ or the absolute sum of the eigenvalues of ρ^Γ . For practical and numeric calculations it is often more easy and stable to take a single eigenvalue than the need to compute the sum of multiple. For all numerical calculations in this thesis, I therefore opt for an alternative way to compute the logarithmic negativity.

Lemma 2.1. *The trace norm $\|A\|_1 \equiv \text{tr} \sqrt{A^\dagger A}$ of a hermitian matrix A is equal to the sum of the absolute eigenvalues of A .*

Proof. This can be immediately seen by the spectral decomposition $\lambda(A) = \{\lambda_1, \dots\}$:

$$\text{tr} \sqrt{A^\dagger A} = \text{tr} \sqrt{A^2} = \text{tr} \left\{ U \sqrt{\text{diag}(\lambda_1, \dots)^2} U^\dagger \right\} = \sum_i \sqrt{\lambda_i^2} = \sum_i |\lambda_i|.$$

\square

Proposition 2.3. *The negativity eq. (2.20) is given as the absolute sum of all negative eigenvalues of ρ^Γ :*

$$\mathcal{N}(\rho) \equiv \frac{\|\rho^\Gamma\|_1 - 1}{2} = \left| \sum_{\lambda_i < 0} \lambda_i \right|. \quad (2.22)$$

Proof. The proof is in parts given by Vidal and Werner [18]. It is known that the density matrix is hermitian: $\rho = \rho^\dagger$. Using lemma 2.1, the trace norm of the density matrix is given as $\|\rho\|_1 = \sum \lambda_i = \text{tr} \rho = 1$. The partial transpose ρ^Γ obviously also satisfies $\text{tr} \rho^\Gamma = 1$ but might have negative eigenvalues. Since ρ^Γ is still hermitian, the trace norm is given by

$$\|\rho^\Gamma\|_1 = \sum_i |\lambda_i| = \sum_{\lambda_i \geq 0} \lambda_i + \sum_{\lambda_i < 0} |\lambda_i| = \sum_i \lambda_i + 2 \sum_{\lambda_i < 0} |\lambda_i| = 1 + 2 \sum_{\lambda_i < 0} |\lambda_i|,$$

where in the last step $\sum \lambda_i = \text{tr} \rho^\Gamma = 1$ was used. \square

Remark. The PPT criterion states, that if ρ^Γ has negative eigenvalues, the state ρ is entangled. The negativity uses this criterion for a quantification of entanglement. This proposition makes sense of the name *negativity*.

Calculating the logarithmic negativity of the evolved state eq. (2.13), it is possible to quantify how the entanglement behaves in time. A straight forward computation following the calculation methods established above yields (for detailed calculations see appendix A.2)

$$E_N(|\psi(t)\rangle\langle\psi(t)|) = \log_2(1 + |\sin \Delta\phi|). \quad (2.23)$$

It is interesting to see, that the maximum entanglement $E_N = 1$ is reached for $\Delta\phi = 2\pi k \pm \pi/2$, $k \in \mathbb{Z}$ and no entanglement ($E_N = 0$) is measurable for $\Delta\phi = k\pi$. This result aligns with the previous observations by demanding that the evolved state eq. (2.13) is separable. The complete entanglement dynamics are shown in fig. 2.2. The time

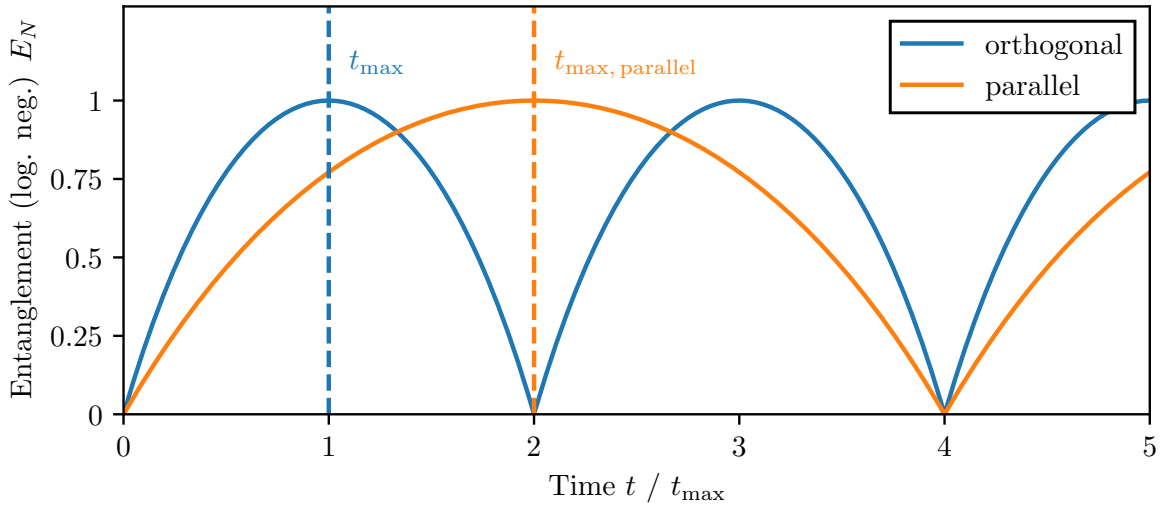


Figure 2.2: Entanglement dynamics quantified by the logarithmic negativity for two different orientations of the spatial superpositions. The parallel orientation was considered in this chapter (see eq. (2.23)), the “orthogonal” one in Ref. [10]. The time of maximum entanglement t_{\max} for the orthogonal configuration is reached after $t_{\max} = 4\pi\hbar L^3/(GM_A M_B \Delta x^2) \simeq 129$ ms.

$t_{\max, \text{parallel}}$ at which the entanglement is maximal (for the first time) can be calculated by using the definition of $\Delta\phi$ from eq. (2.15) as

$$t_{\max, \text{parallel}} = \frac{8\pi L^3 \hbar}{GM_A M_B (\Delta x)^2}. \quad (2.24)$$

In fig. 2.2 the entanglement dynamics for a different orientation considered in Ref. [10] is also shown. There, the superpositions are aligned in the same line as the direct connection between the masses (“orthogonal” to the parallel configuration before), maximizing the differences in distances between them and thus creating entanglement faster. This

expected behavior can be well seen in fig. 2.2: The time t_{\max} until the maximum entanglement is reached, is precisely by a factor of 2 faster than in the here considered parallel configuration [10]. For a practical experiment, this suggests that using the orthogonal orientation could be beneficial and would require shorter coherence times for the superpositions. To give an estimate, consider two identical silica spheres with a density of $\rho = 2648 \text{ kg/m}^3$ with a radius of $R = 10^{-5} \text{ m}$, a separation of $2L = 4R$ and a superposition size $\Delta x = 100 \text{ nm}$ (which is realistic considering theoretical sizes of up to micrometers [6]), the maximum entanglement is reached after about $t_{\max} \approx 129 \text{ ms}$ which is a quite long coherence time and challenging experimentally.

2.3 Issues with the experimental procedure

Additional effects: - Casimir forces entangle as well - Coulomb forces

-j solution: conducting faraday shield, UV discharge [20]

How to measure? Many measurements are necessary -j Entanglement witness? Measure density directly -j Small variations for each measurement in angle of the superposition and in distance to the newly introduced shield

As a estimation of the minimal separation distance L_{\min} , requiring that the gravitational potential should be stronger by a factor χ than the Casimir potential between the two massive spherical particles [21], the following inequality can be stated:

$$\chi |V_{\text{Casimir}}| \leq |V_{\text{Gravity}}| \quad (2.25)$$

$$\chi \times \frac{23\hbar c}{4\pi L^7} \left(\frac{\varepsilon_r - 1}{\varepsilon_r + 2} \right)^2 R^6 \leq \frac{GM^2}{L}. \quad (2.26)$$

Using $M = 4/3\pi R^3 \rho_{\text{Silica}}$, this results in a minimum separation distance independent of the size of the particles of

$$L_{\min} \geq \left(\chi \times \frac{207}{64} \frac{\hbar c}{\pi^3 G \rho_{\text{Silica}}^2} \right)^{1/6} \approx 140 \mu\text{m} \times \sqrt[6]{\chi}. \quad (2.27)$$

3 Casimir effect

Casimir forces can be viewed in a very similar way to the *van der Waals forces*. In fact, both phenomena describe just two different sides of the same coin. They define the so-called ***dispersion forces*** between neutral atoms or bodies. The quantum theory of van der Waals forces between two neutral atoms was developed by London in 1930 who found the attractive potential $\propto 1/r^6$ for small separations [22]. Casimir and Polder showed in 1948, that for separations larger than the resonance wavelength of the atoms, retardation effects need to be taken into account and the potential decays by a power law of $1/r^7$ [16]. Additionally, they calculated the interaction with a atom or molecule and a perfectly conducting plate, showing that macroscopic objects could experience these ***Casimir-Polder interactions*** as well. It becomes evident, that a full description of dispersion forces cannot be given by classical electrodynamics alone. Additional considerations regarding relativistic effects and quantum electrodynamics have to be made [23–25]. Casimir, following a suggestion by Bohr [26], found a simple derivation using the zero-point energy of the vacuum to calculate the attraction between two conducting plates. In quantum electrodynamics each point in the electromagnetic field can be described by an quantized harmonic oscillator with ground state energy $E_0 = \hbar\omega/2$. The total *zero-point energy* of the ground state of the field (the vacuum) is therefore given by summing over the energies E_0 for each possible mode n

$$E_{\text{vacuum}} = \frac{\hbar}{2} \sum_n \omega_n. \quad (3.1)$$

These sums are clearly divergent since there are infinitely many possible excitations. Electrostatic boundary conditions require the field to be zero at the surface of conductors restricting the possible modes between two parallel plates. Precisely the finite difference between the infinite vacuum energy with and without the macroscopic plates give rise to the ***Casimir forces***. Often, this divergence is simply dripped, motivated by the fact that energy is normally defined only up to a constant [23]. Casimir was able to use regularization techniques to deal with the infinite quantities and arrived at his famous formula [15]

$$E_{\text{Casimir}} = -\frac{\hbar c \pi^2}{720 L^3} A. \quad (3.2)$$

for the attractive Casimir-potential between two plates with area A and separation L . The attractive force $F = -\nabla E$ between the plates can now be simply expressed as

$$F_{\text{Casimir}} = -\frac{\hbar c \pi^2}{240 L^4} A. \quad (3.3)$$

3 Casimir effect

It is remarkable, that such a simple relation arises out of the infinities of the vacuum. Up until now, these Casimir forces are topic of modern scientific research. They are generally very difficult to calculate for other geometries than two infinitely large plates or for real materials with dielectric properties. For simple geometries, even the sign of the force is not always intuitively clear: As an example, the Casimir force can be repulsive for an ideal metal spherical shell [24]. For other simple and important bodies like the sphere-plane or sphere-sphere geometry, no universally valid formula for any separation between the bodies exists. This is discussed in more detail in section 3.2.

Almost ten years after the discovery of Casimir and Polder, Lifshitz was the first to find an expression for the Casimir force between two dielectric plates with arbitrary relative permittivity $\varepsilon_{r,1,2}$ for separations larger than the resonant wavelength⁵ [28]. The expression he found facilitates the general complexity of the Casimir interactions and is only expressible as a complicated integral [28]

$$F/A = -\frac{\hbar c}{32\pi^2 L^4} \int_0^\infty dx \int_1^\infty dp \frac{x^3}{p^2} \left\{ \left[\frac{(s_1 + p)(s_2 + p)}{(s_1 - p)(s_2 - p)} e^x - 1 \right]^{-1} + \left[\frac{(s_1 + \varepsilon_{r,1}p)(s_2 + \varepsilon_{r,2}p)}{(s_1 - \varepsilon_{r,1}p)(s_2 - \varepsilon_{r,2}p)} e^x - 1 \right]^{-1} \right\} \quad (3.4)$$

with

$$s_{1,2} = \sqrt{\varepsilon_{r,1,2} - 1 + p^2}.$$

In the limit of two perfectly conducting plates ($\varepsilon_{r,1} = \varepsilon_{r,2} \rightarrow \infty$), the integral can be solved analytically and one gets the same expression already obtained by Casimir

$$F_{\text{cond.}}/A = -\frac{\hbar c}{16\pi^2 L^4} \int_0^\infty dx \int_1^\infty dp \frac{x^3}{p^2(e^x - 1)} = -\frac{\hbar c \pi^2}{240 L^4}. \quad (3.5)$$

Lifshitz determined the Casimir force between a conducting metal plate and a dielectric plate (denoted DM) as well as the force between two dielectric plates with the same dielectric constant ε_r (DD) as

$$F_{\text{DM}} = -\frac{\hbar c \pi^2}{240 L^4} \frac{\varepsilon_r - 1}{\varepsilon_r + 1} \varphi(\varepsilon_r) \quad (3.6)$$

$$F_{\text{DD}} = -\frac{\hbar c \pi^2}{240 L^4} \left(\frac{\varepsilon_r - 1}{\varepsilon_r + 1} \right)^2 \varphi(\varepsilon_r) \quad (3.7)$$

where $\varphi(\varepsilon_r)$ is a numerical function obtained by solving eq. (3.4), which approaches 1 for a perfect conductor. I calculated the function numerically and the result is shown in fig. 3.1. For a dielectric and metal plate, the function φ approaches the finite value $\varphi(\varepsilon_r \rightarrow 1) \approx 0.46$ for small dielectric constants. However, this limit is practically already reached at $\varepsilon_r \approx 4$ and φ stays approximately constant for smaller ε_r .

⁵The “resonance wavelength” for a macroscopic body in this case can be understood as e.g. the plasma frequency in the Drude model [27]. Different models for light-matter interaction result in slightly different resonant wavelength. The Lifshitz formula however holds true for the cases of separations in the micro-meter regime for all practical materials [20].

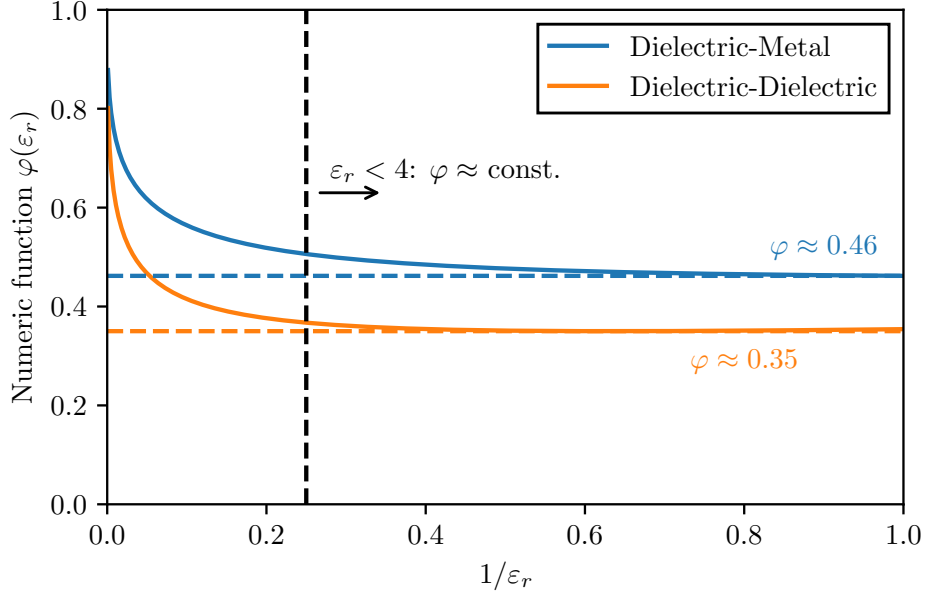


Figure 3.1: Numeric calculations of the function $\varphi(\varepsilon)$ used in the Lifshitz formula eq. (3.6) and (3.7). The function was calculated for **(blue)** a dielectric and a metal plates and **(orange)** two dielectric plates. The function approaches unity for $\varepsilon_r \rightarrow \infty$ and a finite value for $\varepsilon_r \rightarrow 1$.

3.1 Proximity force approximation

The Casimir-Polder force cannot be computed easily for different shapes. There even exists no analytic expression for the simple (and for this thesis relevant) plate-sphere geometry for all ratios L/R and plate-sphere separations. For a general shape, even the sign of the force, i.e. whether it is attractive or repulsive, is often unknown. Fortunately, approximation methods exist and in particular the **proximity-force-approximation (PFA)** can be calculated very easily [29–31]. The PFA is only valid for small separations ($L/R \approx 1$) between the considered smooth bodies. The idea of this approximation is to divide the surfaces of the two bodies into infinitesimal small parallel plates with area dA and summing over the forces dF (or the Casimir-energy dE) between them (see fig. 3.2):

$$E_{\text{PFA}} = \iint_A dA \frac{E_{\text{plate-plate}}}{A} \quad (3.8)$$

where for the casimir energy per unit area $E_{\text{plate-plate}}/A$ either eq. (3.2) or any of the Lifshitz equations (3.7), (3.6) can be chosen. For the following calculations, it is important to distinguish between the distance between the plates center and the spheres center L (like used before) and the edge-to-edge distance $\mathcal{L} = L - R$.

The problem with this approximation is, that it is ambiguous, what surface the area element dA represents. For the plate-sphere geometry, the element can be either chosen tangential to the sphere or parallel to the plate (or in theory any other fictitious surface

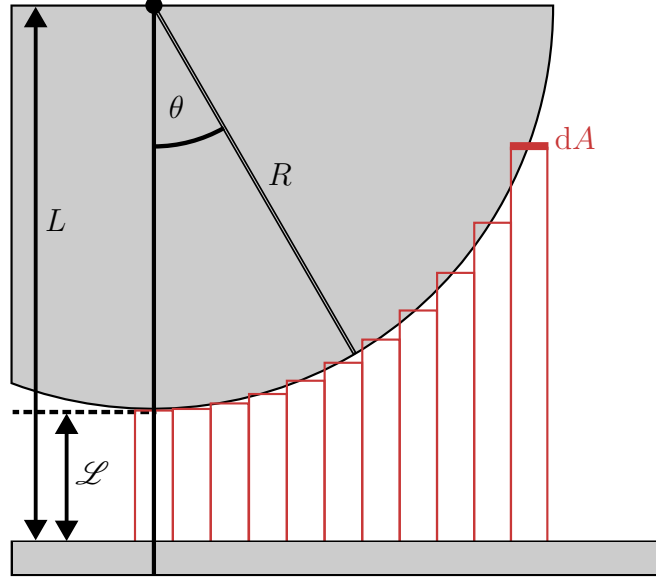


Figure 3.2: In the proximity force approximation the sphere is divided into infinitesimal plane areas dA which all exert a force dF according to eq. (3.3). All the contributions are added up together.

somewhere in between) [31]. For the plate-sphere geometry, in the limit of the validity of the PFA $\mathcal{L} \ll R$ both methods yield the same result. For the following calculations, I choose dA parallel to the plate and the area can be parameterized with $r \in [0, R]$ and $\varphi \in [0, 2\pi]$ resulting in a distance z between the infinitesimal area elements $z(r) = \mathcal{L} + R - \sqrt{R^2 - r^2}$ ⁶. The PFA eq. (3.8) then yields for a dielectric sphere against a perfectly conducting plate

$$E_{\text{plate-sphere}} = -\frac{\hbar c \pi^2}{720} \left(\frac{\varepsilon_r - 1}{\varepsilon_r + 1} \right) \varphi(\varepsilon_r) \int_0^R dr \int_0^{2\pi} r d\varphi \frac{1}{z(r)^3} \quad (3.9)$$

$$= -\frac{\hbar c \pi^3}{360} \left(\frac{\varepsilon_r - 1}{\varepsilon_r + 1} \right) \varphi(\varepsilon_r) \frac{R^2}{2\mathcal{L}^2(R + \mathcal{L})} \quad (3.10)$$

$$\approx -\frac{\hbar c \pi^3}{720} \left(\frac{\varepsilon_r - 1}{\varepsilon_r + 1} \right) \varphi(\varepsilon_r) \frac{R}{\mathcal{L}^2} \quad (3.11)$$

⁶Taking dA tangential to the sphere, it can be parameterized with $\theta \in [0, \pi/2]$ and $\varphi \in [0, 2\pi]$ resulting in $z(\theta) = \mathcal{L} + R - R \cos \theta$. The PFA eq. (3.8) yields with $dA = R^2 \sin \theta d\theta d\varphi$ the result $\propto \frac{\pi R^2 (R + 2\mathcal{L})}{\mathcal{L}^2 (R + \mathcal{L})^2}$ which in the limit of $\mathcal{L} \ll R$ results in the same expression as eq. (3.11).

3.2 Casimir forces between a conducting plate and a dielectric sphere

An empirical derivation for power law of the casimir energy between a sphere and a conducting plate can be made directly from the energy between two atoms with static polarizability α_i given by Casimir and Polder [16]. They derived an expression for the Casimir-Polder potential of ⁷

$$E = -\frac{23\hbar c\alpha_1\alpha_2}{4\pi L^7}. \quad (3.12)$$

The polarizability of a sphere with radius R is derived in appendix B.1 and is given for an dielectric with ε_r as

$$\alpha_{\text{sphere}} = \left(\frac{\varepsilon_r - 1}{\varepsilon_r + 2} \right) R^3. \quad (3.13)$$

If one atom is now replaced by a conducting sphere ($\varepsilon_r \rightarrow 1$) of radius $\sim L$ (much larger than the atom) with a polarizability of L^3 , it get obvious that between this big sphere and the atom, the energy is given by a power law of $1/L^4$. It is therefore natural to assume, that for a macroscopic sphere and a macroscopic plate, the Casimir energy behaves similar to a $1/L^4$ law - at least for the *large separation limit* (LSL). The exact calculation for this problem is very hard. In fact, no analytic solution is known.

Ford was able to determine an integral expression using a macroscopic approach in 1998 [27]:

$$F = -\frac{\hbar c}{4\pi L^4} \int_0^\infty d\omega \alpha(\omega) [3 \sin 2\omega L - 6L\omega \cos 2\omega L - 6L^2\omega^2 \sin 2\omega L + 4L^3\omega^3 \cos 2\omega L]. \quad (3.14)$$

The expression depends on the polarizability, which is generally not constant for a dielectric. Especially for small separations between the sphere and the plate, this dependence and the non-constant polarizability make this integral nearly unsolvable. For large separations, much larger than the absorption wavelength of the dielectric or much larger than the wavelength corresponding to the plasma frequency in the Drude-Model, the polarizability can be assumed to be static $\alpha = \text{const}$ [20, 27]. In this simplifying case, the integral can be solved using an exponential convergence factor and results in

$$F = -\frac{6\hbar c}{4\pi L^5} \alpha \quad (3.15)$$

and thus

$$E = -\frac{3}{8} \frac{\hbar c}{\pi L^4} \left(\frac{\varepsilon_r - 1}{\varepsilon_r + 2} \right) R^3. \quad (3.16)$$

⁷For two macroscopic spheres, the casimir potential looks very similar to eq. (3.12). The polarizability of a sphere is given by eq. (3.13). Using this result, the Casimir energy between two identical dielectric spheres in the large separation limit is given as $-\frac{23\hbar c}{4\pi L^7} \left(\frac{\varepsilon_r - 1}{\varepsilon_r + 2} \right)^2 R^6$ [21].

For the large separation limit, the Casimir interaction between a sphere and a plate behaves like expected considering the motivation of the $1/L^4$ -law above in this section.

A second method to calculate the Casimir energy for arbitrary compact objects and a conducting wall was developed by Emig *et. al.* [21]. For the sphere-plate geometry, this results in the large separation limit (LSL) in a infinite series, where the first-order term ($\propto 1/L^4$) is precisely given by eq. (3.16) [30, 32]. The first 8 terms of this series are shown in fig. 3.3 as well as a few specific numerical points for higher terms. It becomes

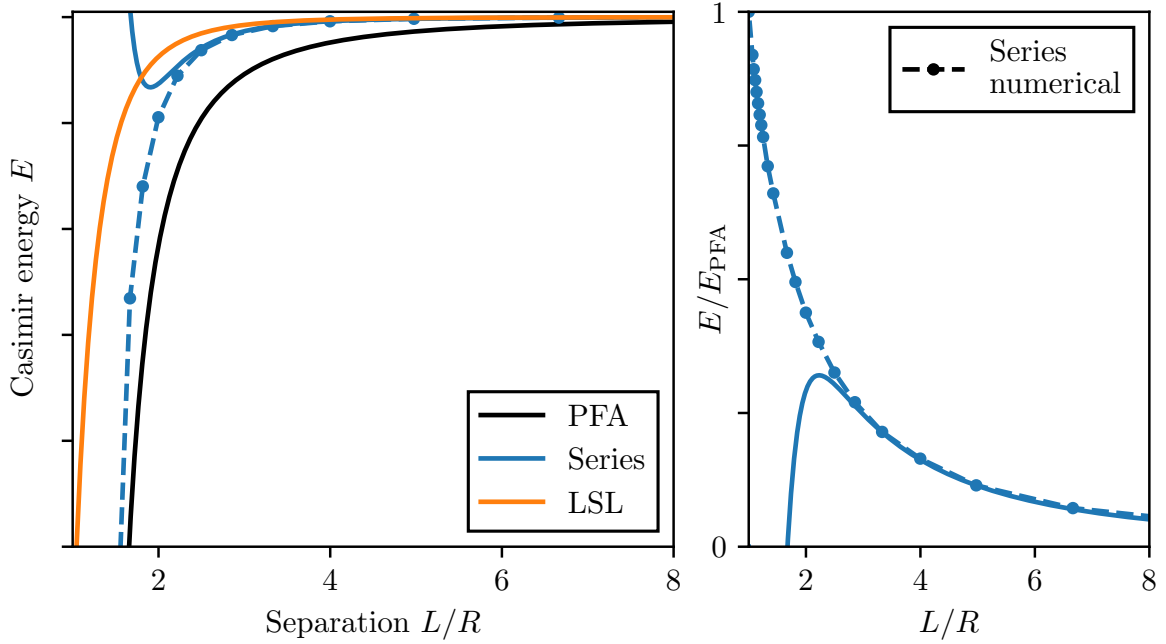


Figure 3.3: Behavior of different approximations of the casimir interaction between a conducting sphere and a perfectly conducting plate. Additionally, a comparison between the PFA and an exact numerical series expansion from Ref. [30] is shown.

evident, that the series expansion converges to the LSL eq. (3.16) for large separations and to the PFA eq. (3.11) for small separations. However, quantitatively the numerics show, that $E/E_{\text{PFA}} \leq 1$ and thus the PFA predicts a stronger Casimir energy for all separations.

Theorem 3.1. *The PFA model for a **conducting sphere** and a conducting plate predicts a stronger casimir energy for all separations L/R than the LSL or the exact series expansion.*

Proof. a) The numerical series expansion in fig. 3.3 from Ref. [30] shows that $|E_{\text{series}}| \leq |E_{\text{PFA}}|$ for all L/R .

b) Comparing the PFA eq. (3.11) for a conducting sphere with a dielectric one, it becomes evident, that $|E_{\text{cond.}}| \geq |E_{\text{diel.}}|$. This can be seen by the fact that for $\varepsilon_r \in [1, \infty)$ $\varphi(\varepsilon_r) \leq 1$ and $(\varepsilon_r - 1)/(\varepsilon_r + 1) \leq 1$. Thus the PFA for conductors is always a worse approximation.

c) Analytically, it can be shown that the energy predicted by the LSL eq. (3.16) is always smaller than the PFA:

$$|E_{\text{PFA}}| > |E_{\text{LSL}}| \quad (3.17)$$

$$\frac{\hbar c \pi^3}{720} \left(\frac{\varepsilon_r - 1}{\varepsilon_r + 1} \right) \varphi(\varepsilon_r) \frac{R}{\mathcal{L}^2} > \frac{3\hbar c}{8\pi L^4} \left(\frac{\varepsilon_r - 1}{\varepsilon_r + 2} \right) R^3 \quad (3.18)$$

$$\frac{8\pi^4}{3 \cdot 720} \frac{\varepsilon_r + 2}{\varepsilon_r + 1} \varphi(\varepsilon_r) > \frac{(L - R)^2 R^2}{L^4} = \left(\frac{R}{L} \right)^2 - 2 \left(\frac{R}{L} \right)^3 + \left(\frac{R}{L} \right)^4 \quad (3.19)$$

Maximizing the RHS, and using the fact that $R/L \leq 1$, the maximum is $1/16$ at $R/L = 1/2$. The minimum of the LHS is a little more complicated. The minimum of $\varphi(\varepsilon_r)$ is reached for $\varepsilon_r = 1$ and is at a minimum 0.46. The minimum of $(\varepsilon_r + 2)/(\varepsilon_r + 1)$ is reached at $\varepsilon_r \rightarrow \infty$ and is 1. Thus the LHS is at the absolute (unreachable) minimum $8\pi^4/2160 \cdot 0.46 \approx 0.166$ which is still larger than $1/16$. \square

Remark. This is rather unintuitive, because one would expect it to be the other way around. The $1/L^4$ dependence in the LSL should - for small separations - tend much faster to zero than the $1/\mathcal{L}^2$ dependence in the PFA. However considering the differences between L and $\mathcal{L} = L - R$, this is no longer surprising.

Admittedly, for separations $L/R \gtrsim 2$, the difference is not very large. Nevertheless will I use the PFA eq. (3.11) for the rest of the thesis as a worst-case estimation. Keep in mind, that the some quantities might be overestimated.

3.3 Imperfect plate and spheres

Python numerical approach, gaussian modes (vibration modes of a spherical plane), perlin noise

- In the worst case like using the maximum of the vibration
- Numerical results suggest, that for very random fluctuations, it is even better (but not always a worst-case approximation) to use the average elevation

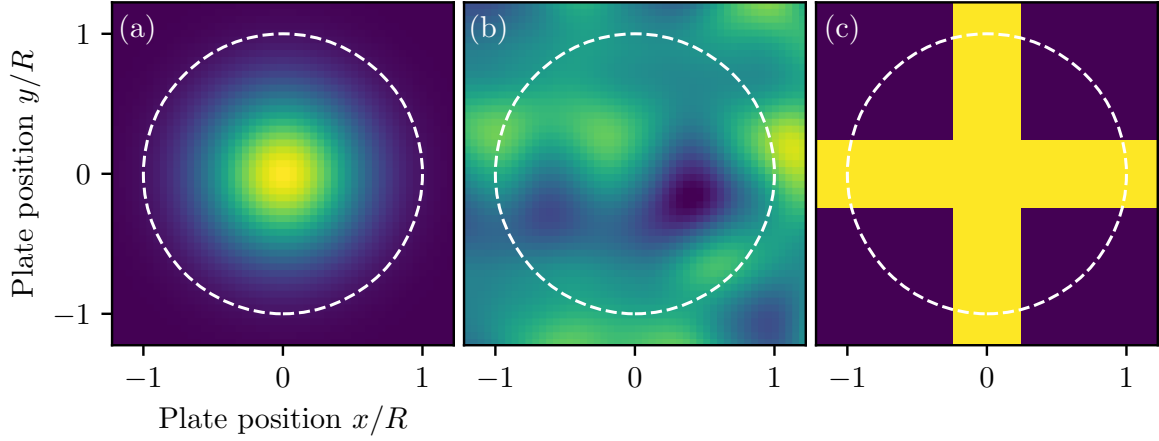


Figure 3.4: A selection of imperfect plates. (a) A simple gaussian displacement in the same size as the sphere. (b) Random excitations in the shape of *perlin noise*. (c) a cross-shape in the center of the plate. All displacements are in the size of $0.1R$.

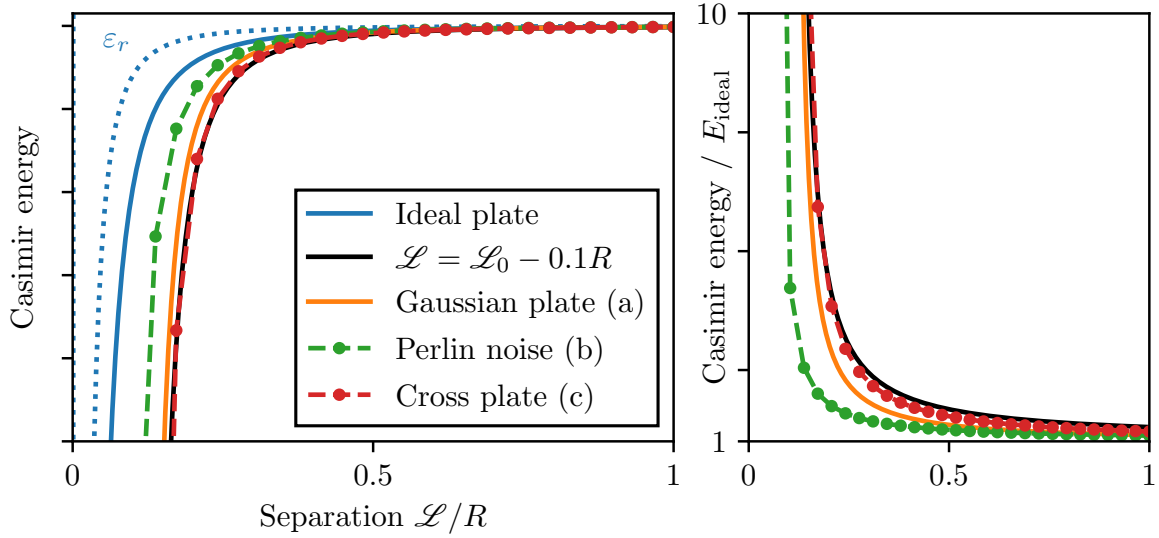


Figure 3.5: Casimir energy for the different noisy plates displayed in fig. 3.4. It becomes evident, that local deviations in the distance between the plate and the sphere in the order of $\Delta\mathcal{L} \sim 0.1R$ increase the Casimir force exponentially for very small separations. Larger separations however are seemingly unaffected.

4 The particle in front of a static shield

The generalized form of the system described in chapter 2 with the addition of a conducting Faraday shield is shown in fig. 4.1. As before, the masses are delocalized in cat-states with superposition separations Δx_A for mass A and Δx_B for mass B respectively. The

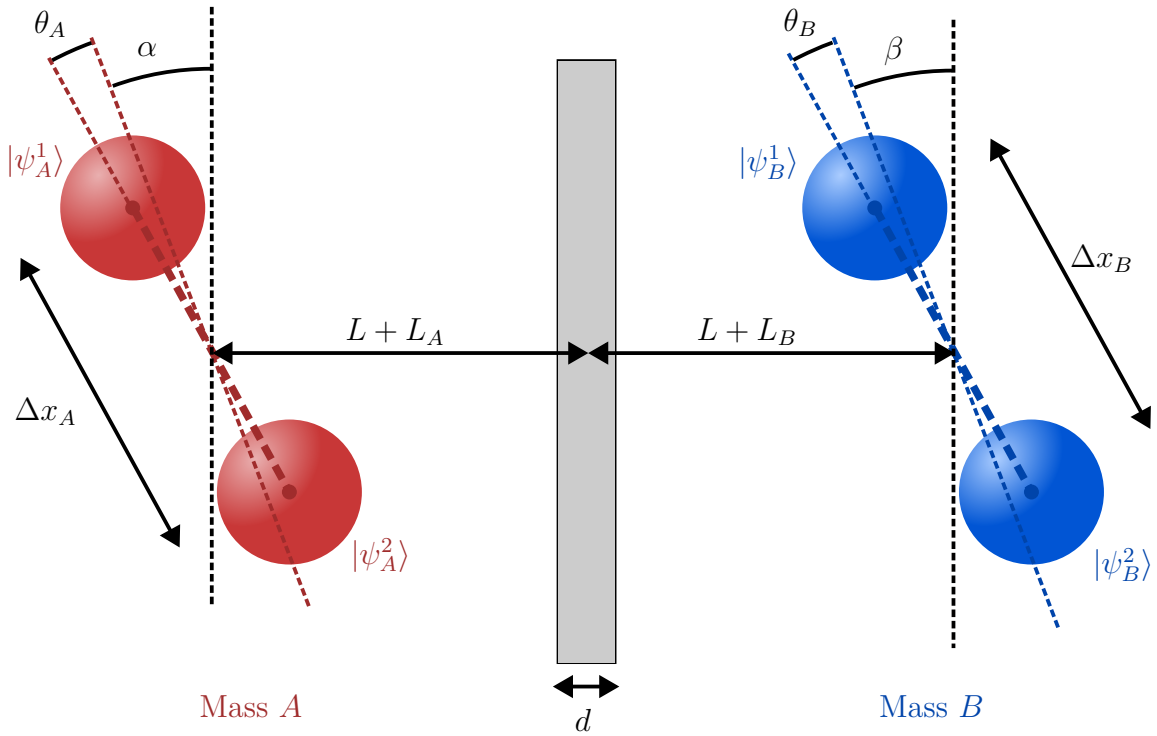


Figure 4.1: Schematic depiction of a experimental setup for the detection of gravitationally induced entanglement between two particles A and B . They are separated by a distance of $2L + L_A + L_B$ in arbitrary orientations given by the angles α and β with small variations $\theta_{A(B)}$. All variations are assumed to be gaussian distributed around mean zero with standard deviation $\Delta L_{A(B)}$ and $\Delta \theta_{A(B)}$. The masses are delocalized in a cat state with a separation $\Delta x_{A(B)}$ between the states $|\psi_{A(B)}^1\rangle$ and $|\psi_{A(B)}^2\rangle$. A conducting Faraday shield with thickness d is placed in the center between the masses.

superpositions are extended in arbitrary orientations α and β (due to symmetries, it is

enough to consider $\alpha, \beta \in [0, \pi)$). Most notably, the orientation of $\alpha = \beta = 0$ represents the same “parallel configuration” discussed earlier. The case of $\alpha = \beta = \pi/2$ is referred to as the “orthogonal orientation”. If gravity is assumed to be able to mediate entanglement, the above system can generate entanglement between both particles A and B due to their mutual gravitational interaction. Placing a Faraday shield in the center between the masses should not influence the gravitational entanglement generation. However, Casimir interactions between the shield and the masses are still present at small separations. It is straightforward to convince yourself that these interactions can only give rise to local phases for each state, dependent only on their associated shield-mass distance. Such local interactions can - assuming a static shield e.g. at zero temperature - not induce any additional entanglement between the masses.

For a complete picture, one has to consider experimental challenges and limitations in a real experiment. Measuring the states after some time evolution to determine their entanglement requires knowledge of the states which can be obtained by e.g. **full state tomography**. Some proposals aim to measure the entanglement using a suitable witness [4, 6], but the creation of such an entanglement witness requires knowledge of the specifics on the experimental realization. In this thesis, I will focus on the most general and universally applicable case of measuring the complete density matrix of the system and checking for entanglement. The density matrix of a 2 qubit system consists of 16 different entries (only 9 of them are independent⁸). Tomography requires a lot of measurements to be made on the system. During these measurements, one cannot be sure that the masses are placed in the exact same position and orientation each run or. Even if it was somehow possible, to place the particle at the *exact* same position each measurement, thermal vibrations of the shield induce small variations over a lot of runs.

Thus, even if the masses get entangled in each run of the measurement, due to the slightly different system measured the result of many measurements looks like a mixed state

$$\rho = \int_{-\infty}^{\infty} d\theta_i \frac{1}{\sqrt{2\pi}\Delta\theta_i} e^{-\theta_i^2/2(\Delta\theta_i)^2} |\psi_\theta\rangle\langle\psi_\theta|. \quad (4.1)$$

Here, $|\psi_\theta\rangle$ is the pure state of a single measurement dependent on the angular variations θ_i ($i = A, B$). These variations are assumed to be gaussian distributed around mean 0 and standard deviation $\Delta\theta_{A,B}$. The same argument can be made for variations in the distance, which are distributed with $\Delta L_{A,B}$. In some cases, as for example if the plate is not placed exactly in the center or at an angle, the variations θ_i and L_i are correlated and $L_A = -L_B$ holds. In the most general case, all variations are assumed to be independent and follow their own probability distribution.

⁸Using the known characteristics of the density matrix like hermiticity $\rho^\dagger = \rho$ and $\text{tr} \rho = 1$, it is possible to reconstruct ρ from only 9 specific entries.

4.1 Entanglement generation

If the state ρ is reconstructed using repeated measurements, but the initial placement of the particles were slightly different for each measurement, this is effectively comparable to an averaging process over all variations of the setup. As mentioned above, this averaging results in a mixed state and for large variations $\Delta\theta$ and ΔL , this process can destroy entanglement. To see this, I calculate the effective measured state $\langle\rho\rangle$ using

$$\langle\rho\rangle = \int_{-\infty}^{\infty} d\theta_A p(\theta_A) \int_{-\infty}^{\infty} d\theta_B p(\theta_B) \int_{-\infty}^{\infty} dL_A p(L_A) \int_{-\infty}^{\infty} dL_B p(L_B) \rho(\theta_A, \theta_B, L_A, L_B) \quad (4.2)$$

where $p(\cdot)$ is the gaussian probability distribution. Both θ and L are distributed normally with mean 0 and standard deviation $\Delta\theta$ or ΔL respectively. $\rho(\theta_A, \theta_B, L_A, L_B)$ is the state of a single measurement, dependent on the initial parameters $\theta_{A(B)}$ and $L_{A(B)}$ of the setup. The initial state ρ_0 at $t = 0$ is given similarly as before in eq. (2.7) at the beginning of chapter 2. During time evolution, not only the mutual gravitational interaction between the particles has to be considered, but additionally the dephasing due to the Casimir interaction between the particles and the Faraday shield. A single superposition state $|\psi_{A(B)}^i\rangle$ ($i = 1, 2$) accumulates the phase $\phi_{A(B), \text{Cas}}^i(t)$ during time evolution due to the casimir interaction which is given as

$$\phi_{A(B), \text{Cas}}^i(t) = \frac{t}{\hbar} \begin{cases} \frac{3\hbar c}{8\pi} \left(\frac{\varepsilon_r - 1}{\varepsilon_r + 2} \right) \frac{R^3}{(L_{A(B)}^i)^4} & \text{for large separations (LSL)} \\ \frac{\hbar c \pi^3}{720} \varphi(\varepsilon_r) \left(\frac{\varepsilon_r - 1}{\varepsilon_r + 1} \right) \frac{R}{(\mathcal{L}_{A(B)}^i)^2} & \text{for small separations (PFA)} \end{cases} \quad (4.3)$$

Here, both analytical limits of the Casimir interaction discussed in chapter 3 have been used. The particle-shield separations $L_{A(B)}^i$ and $\mathcal{L}_{A(B)}^i = L_{A(B)}^i - R$ are dependent on the initial (varying) positions of each particle. In full generality, they are given by

$$L_{A(B)}^i = L + L_{A(B)} - \frac{d}{2} \pm \frac{\Delta x_{A(B)}}{2} \sin(\delta + \theta_{A(B)}) \quad (4.4)$$

where \pm distinct between $i = 1$ and $i = 2$ and $\delta = \alpha, \beta$ was used as an abbreviation. The mutual gravitational interaction of the state $|\psi_A^i\rangle \otimes |\psi_B^j\rangle$ is given similar to before by the accumulated phase

$$\phi_{\text{Grav}}^{ij}(t) = \frac{t}{\hbar} \frac{GM_A M_B}{L^{ij}}. \quad (4.5)$$

The separation distance L^{ij} between the masses A_i and B_j in full generality is given by

$$L^{ij} = \sqrt{\left(2L + L_A + L_B \pm \frac{\Delta x_A}{2} \sin(\alpha + \theta_A) \mp \frac{\Delta x_B}{2} \sin(\beta + \theta_B)\right)^2 + \left(\frac{\Delta x_A}{2} \cos(\alpha + \theta_A) \pm \frac{\Delta x_B}{2} \cos(\beta + \theta_B)\right)^2}. \quad (4.6)$$

Expanding the accumulated gravitational- and Casimir phases to first order in $\Delta x_{A(B)} \ll L$, $\theta_{A(B)} \ll 1$ and $L_{A(B)} \ll 1$ (which is possible since all these variations are very small,

as seen later), the averaging of the evolved state $\langle rho \rangle$ eq. (4.2) can be performed analytically (for an exemplary calculation see appendix D). It turns out that with $\Delta\theta_A = \Delta\theta_B \equiv \Delta\theta$ and $\Delta L_A = \Delta L_B \equiv \Delta L$ all off-diagonal elements of the averaged state $\langle \rho \rangle$ (the so-called **coherences**) are given in the form

$$\langle \rho_{kl} \rangle = \frac{1}{4} e^{i\Delta\phi_{kl}(t)} \exp\left\{-\frac{(\Delta\theta)^2}{2} (\Delta\phi_{kl,\theta})^2 t^2\right\} \exp\left\{-\frac{(\Delta L)^2}{2} (\Delta\phi_{kl,L})^2 t^2\right\} \quad (4.7)$$

where all $\Delta\phi$ -terms are substitutes for rather lengthy phase expressions that depend on the particle-shield separation L , the orientation of the cat-state α, β , the masses of the particles $M_{A(B)}$ and the superposition size $\Delta x_{A(B)}$. It becomes evident that for large times $t \rightarrow \infty$ or for large variations in the placement $\Delta\theta, \Delta L \rightarrow \infty$ these off-diagonal elements tend to zero which leads to a continuous and monotonic loss of purity, resulting in the maximally mixed state $\text{tr} \rho^2 = 1/4$ - which obviously is not entangled. For large variations in the placement of the particles, one therefore expects the loss of coherence and thus of entanglement.

The resulting logarithmic negativity of the averaged state $E_N(\langle \rho \rangle)$ was computed numerically for different values of $\Delta\theta$ and ΔL and is shown in fig. 4.2. For this figure, the parallel orientation $\alpha = \beta = 0$ was used at times given by the time of maximum entanglement t_{max} from eq. (2.24). The radius of the particles was set to $R = 1 \times 10^{-5}$ m with corresponding mass $M_A = M_B = 4/3 \pi R^3 \rho_{\text{Silica}} \approx 1.1 \times 10^{-11}$ kg. A particle-shield separation of $L = 2R$ and a superposition size of $\Delta x_A = \Delta x_B = 100$ nm were chosen. In the rest of the thesis, if not otherwise specified, these parameters are used as a default. They are chosen in the specific orders of magnitude, because they result in a feasible low experiment-time $t_{\text{max}} \approx 258$ ms and are in the region of what is soon⁹ possible [33]. It is important however to stress out, that all these parameters are orders of magnitude away of from what is experimentally reachable today. The largest mass that was studied in matter-wave interferometry is in the order of 4×10^{-23} kg [13] with an superposition size of $\Delta x \gtrsim 500$ nm. For solid state mechanical systems quantum control and in particular groundstate cooling up to masses in the order of 10^{-13} kg [34], 10^{-11} kg [35] and 10^{-8} kg [36] with very short coherence times $\lesssim 1 \mu\text{s}$ have been demonstrated. On the contrary, the smallest mass with a measurable gravitational coupling is around 92 mg [14]. Levitated particles combine the best of both world with quantum control of large and heavy trapped solid objects as well as long coherence times up to the order of seconds [33].

The entanglement of the system shown in fig. 4.2 behaves as expected. At some critical point $\Delta\theta_{\text{crit}}$ and ΔL_{crit} , the entanglement is completely lost. For the used parameters and in the parallel orientation, this threshold is around $\Delta\theta_{\text{crit}} \approx 6 \times 10^{-10}$ rad and $\Delta L_{\text{crit}} \approx 1.4 \times 10^{-10}$ m, which seems quite challenging experimentally. However, it seems like that for smaller times $t < t_{\text{max}}$ larger variations can be tolerated for the cost of having less total entanglement. This again is expected. For smaller times, the gravitational force did not have enough time to fully entangle the two particles, but also the decoherences (dependent on $\propto t^2$; see eq. (4.7) and appendix D) did not have enough

⁹“Soon” in this context means still a long time, but the experiment could be doable within this century.

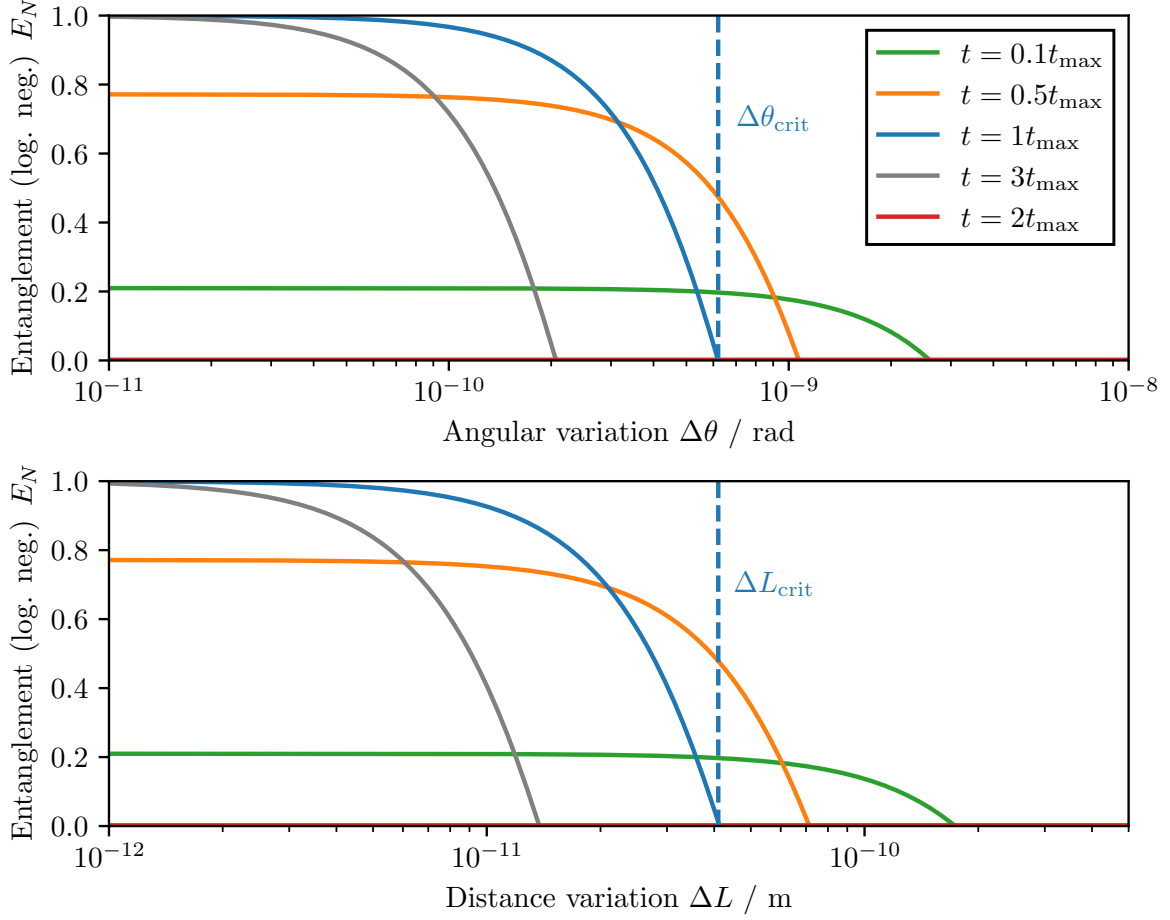


Figure 4.2: Entanglement quantified by the logarithmic negativity (eq. (2.21)) dependent on the angular variation $\Delta\theta$ and the distance variation ΔL in the parallel configuration. The entanglement is shown at different times, where $t_{\text{max}} \approx 258$ ms is the time of maximal entanglement from eq. (2.24). At the critical point $\Delta\theta_{\text{crit}}$ or ΔL_{crit} all entanglement is lost.

time to built up. It is therefore logical, that if one does not require to measure a fully entangled state and less entanglement $E_N < 1$ is also sufficient, it may be beneficial to measure at a time $t < t_{\text{max}}$. In theory, it would be enough to measure *any* entanglement $E_N > 0$ but one has to make sure that no other mechanisms such as direct or indirect entanglement trough other couplings or noise sources have smaller entanglement rates (for a discussion see chapter 5). Measuring at a earlier point in time does not only reduce the duration of a single experimental measurement, but also increases the stability against displacement variations. This optimal time of measuring for a certain required amount of entanglement is shown in fig. 4.3. The chart additionally lets one read out the corresponding maximal angular variation after a set time. Conversely, if one is experimentally limited by a certain maximum angular variation, one can read off the corresponding best measurement time and the maximum amount of entanglement that

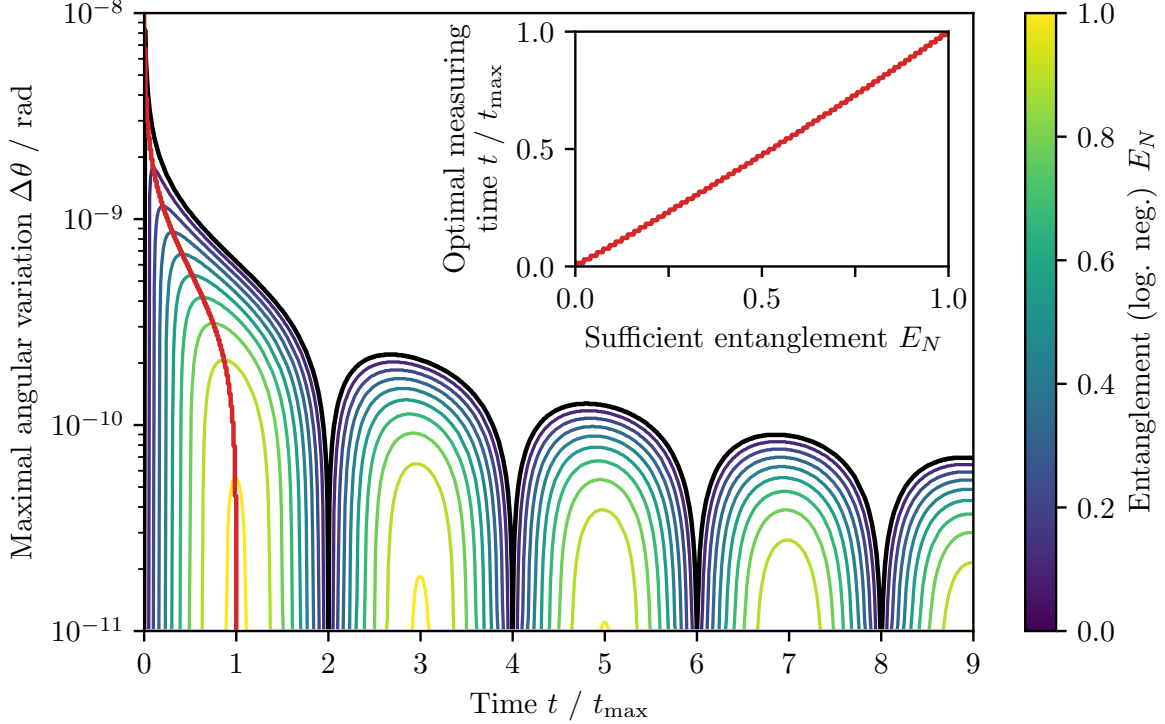


Figure 4.3: Maximal angular variation for a given time and a given required amount of entanglement. The outer most black line corresponds to the time dependence of $\Delta\theta_{\text{crit}}$. The top left as well as the red curve in the main figure shows the optimal measuring time for a sufficient amount of entanglement. At times $2kt_{\text{max}}$ no entanglement can be measured.

can be obtained. It also can be seen that at times $2kt_{\text{max}}$, $k \in \mathbb{N}$ there is no entanglement. This corresponds to the findings from the ideal scenario in chapter 2.

4.2 The optimal setup

With the general framework in hand, the next logical question to ask is, if the stability against placement-variations can be improved. The general rule of thumb for these optimizations is the following: Increase the gravitational interaction by either heavier and larger particles or by reducing the separation distance L without substantial sacrifices of experimental realization. As an example, the stability increases intuitively by increasing the separation distance L . However, this does also increase the time t_{max} until the maximum amount of entanglement can be measured which would increase the total time $\sim \#t_{\text{max}}$ of the experiment with $\#$ individual measurements. It is not immediately obvious, how the stability and the maximum possible variations $\Delta\theta_{\text{crit}}$ and ΔL_{crit} behave for the change in parameters. In the following section, precisely the changing of

this stability is discussed for changing the orientation α, β , the separation L , the mass $M_A = M_B \equiv M$ and the superposition size $\Delta x_A = \Delta x_B \equiv \Delta x$.

4.2.1 Orientation

The arguably easiest parameter to change experimentally is the orientation of the superpositions, which is quantified by α and β in fig. 4.1. As already seen in fig. 2.2, the entanglement dynamics are dependent on the orientation. In the parallel orientation, the states take twice as long as in the orthogonal orientation to become maximally entangled. In general, it is advantageous to aim for the highest entanglement rate and thus the smallest $t_{\max}(\alpha, \beta)$, as this requires a shorter coherence time and thus reduces the total time of the experiment. The previous results from chapter 2 can be further generalized for an arbitrary orientation α, β . The logarithmic negativity is given by

$$E_N = \log_2 (1 + |\sin \Delta\phi|) \quad (4.8)$$

where $\Delta\phi$ is now dependent on the orientation and is defined as (for $\Delta x \ll L$)

$$\Delta\phi = \frac{GM_A M_B t \Delta x_A \Delta x_B}{8\hbar L^3} \left(\sin \alpha \sin \beta - \frac{1}{2} \cos \alpha \cos \beta \right). \quad (4.9)$$

The maximum entanglement $E_N = 1$ is reached for $\Delta\phi = \pm\pi/2$ and thus after a time

$$t_{\max}(\alpha, \beta) = \frac{4\pi\hbar L^3}{GM_A M_B \Delta x_A \Delta x_B} \left| \sin \alpha \sin \beta - \frac{1}{2} \cos \alpha \cos \beta \right|^{-1}. \quad (4.10)$$

For some specific symmetric cases, the resulting times for different orientations are shown in fig. 4.4. The global minima of $t_{\max}(\alpha, \beta)$ is attained in the orthogonal orientation. This is not surprising considering that this orientation maximizes the *differences in separation distances* between all superposition states. Much more interesting and surprising are the unanticipated singularities in fig. 4.4 which appear for

$$\sin \alpha \sin \beta = \frac{1}{2} \cos \alpha \cos \beta. \quad (4.11)$$

For $\beta = 0$ the singularity at $\alpha = \pi/2$ is not surprising. In this configuration, the distances $|\psi_A^1\rangle \leftrightarrow |\psi_B^{1,2}\rangle$ and $|\psi_A^2\rangle \leftrightarrow |\psi_B^{1,2}\rangle$ are identical and thus these states accumulate the same phases, resulting in a factorable global phase. In the case of $\alpha = \beta$, the two singularities are precisely given in the orientation

$$\alpha = \beta = 2 \arctan(\sqrt{3} \pm \sqrt{2}) \approx 90^\circ \pm 54.74^\circ. \quad (4.12)$$

There does not exist a straight-forward geometric interpretation why no entanglement is generated exactly in this configuration, however all 4 separation distances between the states form the “harmonic mean” visualized in fig. 4.5. Here, in the limit $\Delta x \ll L$ everything local phase precisely cancels out resulting in a loss of entanglement. To avoid

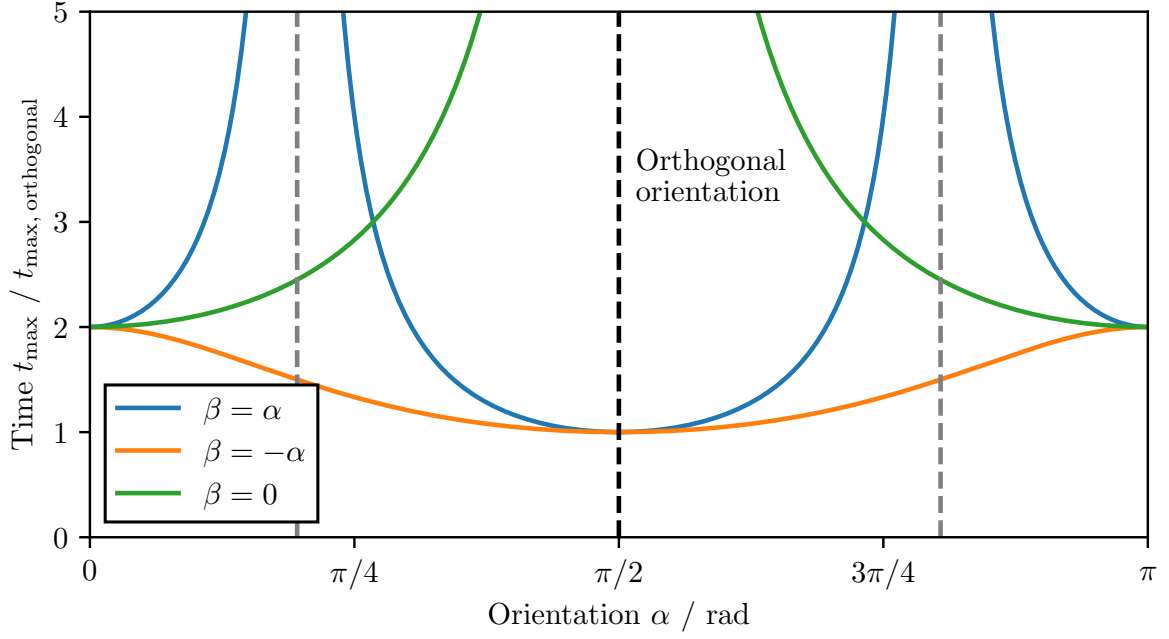


Figure 4.4: Time t_{\max} after which maximum entanglement ($E_N = 1$) is reached for different orientations. Only the most interesting and highly symmetric cases $\alpha = \pm\beta$ and $\beta = 0$ are shown. The singularity $t_{\max} \rightarrow \infty$ for $\beta = 0$ and $\alpha = \pi/2$ is expected. The two other singularities at $\alpha = \beta = 2 \arctan(\sqrt{3} \pm \sqrt{2})$ are explainable by the “harmonic mean” in fig. 4.5.

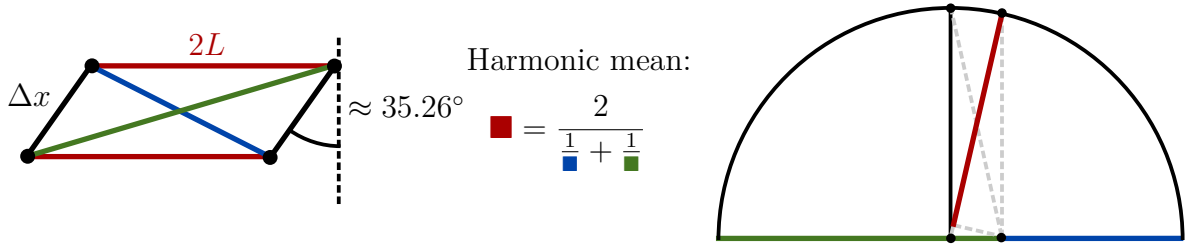


Figure 4.5: left: The system in the orientation $\alpha = \beta = 2 \arctan(\sqrt{3} - \sqrt{2})$. For $\Delta x \ll L$, all separation distances exactly form the *harmonic mean*. Here, the phases due to the mutual gravitational interaction precisely cancel out resulting in no entanglement. **right:** Geometric visualization of the harmonic mean.

all these singularities, it is advisable to always take $\alpha = -\beta$, where all orientations result in roughly similar entanglement times t_{\max} , at most only differing by a factor of 2.

It should come as no surprise that the different orientations exhibit different stabilities. Logically, one would expect the orthogonal configuration to be much more sensitive to angular variations than the parallel one. In contrary, the parallel configuration should be much more stable against variations in the distance, since no phase difference (“dephasing”) is induced between the two superposition states $|\psi_{A(B)}^1\rangle$ and $|\psi_{A(B)}^2\rangle$ of the particle A (B).

The effect of different orientations on the stability against angular variations and the behavior of the critical angular variation $\Delta\theta_{\text{crit}}$ is shown in fig. 4.6. As expected, the

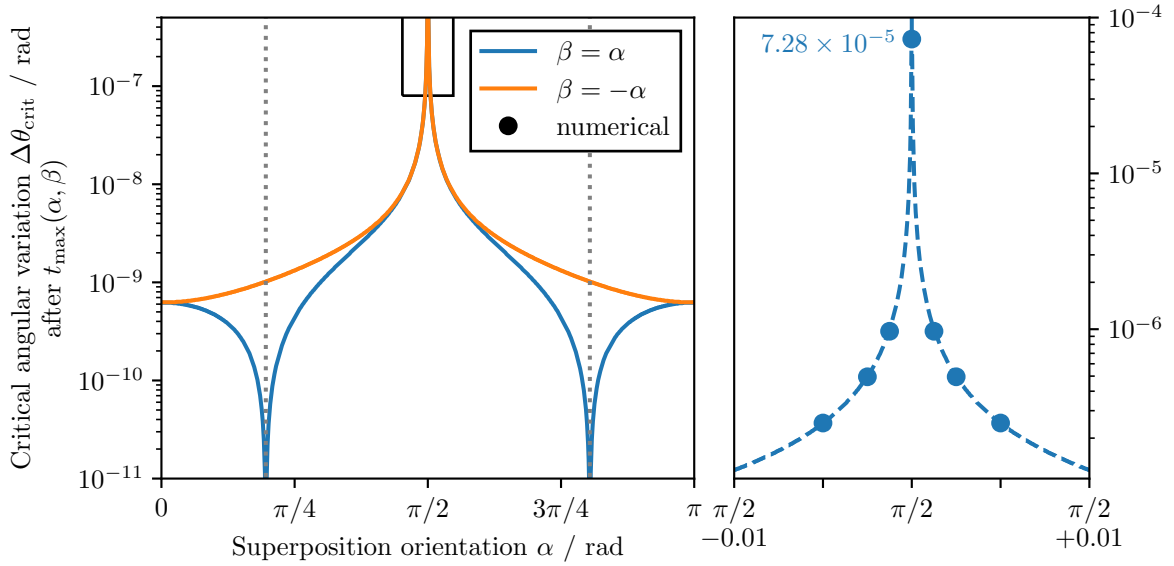


Figure 4.6: Critical angular variation $\Delta\theta_{\text{crit}}$ for different orientations after the time $t_{\max}(\alpha, \beta)$ for which maximum entanglement is reached. The **orthogonal orientation** magnified on the right is very stable against angular variations and only numerical methods show a finite stability value. The singularities in the left figure for $\alpha = \beta$ arise from the fact, that these orientations need infinite time to entangle as already seen in fig. 4.4.

orthogonal configuration is the most stable against these kind of variations. This is, because the dephasing ultimately depends on the distance between the state and the shield $L \pm \Delta x/2 \cos \theta \approx L \pm \Delta x/2(1 - \theta^2/2)$, which is a only second order effect of the angular variations θ . This explains the apparent “infinitely” good stability in the figure, as the analytical solution only uses first order approximations in θ . Exact numerical results however cap the stability at $\Delta\theta_{\text{crit, orthogonal}} \approx 7.3 \times 10^{-5}$ rad.

Respectively, the stability against distance variations ΔL_{crit} for different orientations is shown in fig. 4.7. Again aligning with expectations, the parallel configuration is (in theory) exhibits an infinite stability. One however could argue, that a for this to hold,

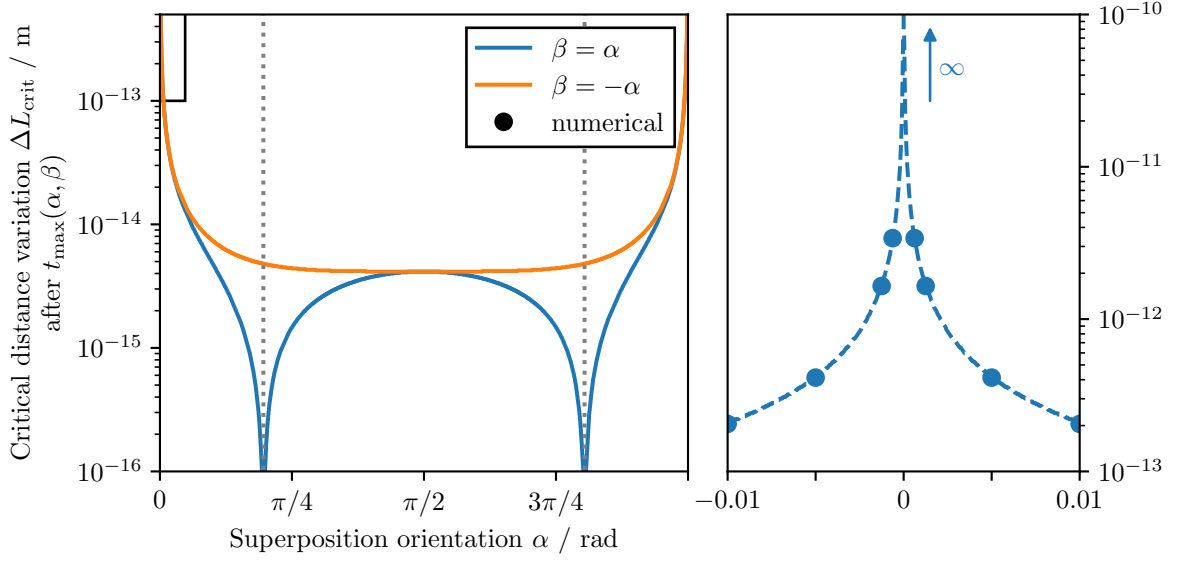


Figure 4.7: Critical distance variation ΔL_{crit} for different orientations after a time $t_{\text{max}}(\alpha, \beta)$. Here, the **parallel orientation** (magnified on the left) is infinitely stable against placement variations.

the uncertainties in the angular placement have to be zero. As could be seen in fig. 4.6, these variations are at most around $\sim 5 \times 10^{-5}$ rad and thus a realistic upper bound for the minimum required distance variations is given by $\Delta L_{\text{crit,parallel}} = \Delta L_{\text{crit}}(\alpha \approx 5 \times 10^{-5} \text{ rad}) \simeq 4 \times 10^{-11} \text{ m}$. It is important to keep in mind, that these stability values can be improved substantially by changing e.g. the separation distance L or the particle size R .

Considering these results, the parallel orientation seems to be the only realistic experimental option, even if it requires slightly larger coherence times t_{max} . Keeping particle-shield separation variations below 0.01 nm - approximately the size of a single atom - is practically impossible, especially under the additional consideration of the thermal vibrations of the shield and the particles, which are in the same order of magnitude as seen later in chapter 5. With this data on hand, it is possible to generate the stability diagram in fig. 4.8, showing the optimal orientation in which the most entanglement can be measured. For most combinations of ΔL and $\Delta\theta$, entanglement is only given in one certain orientation.

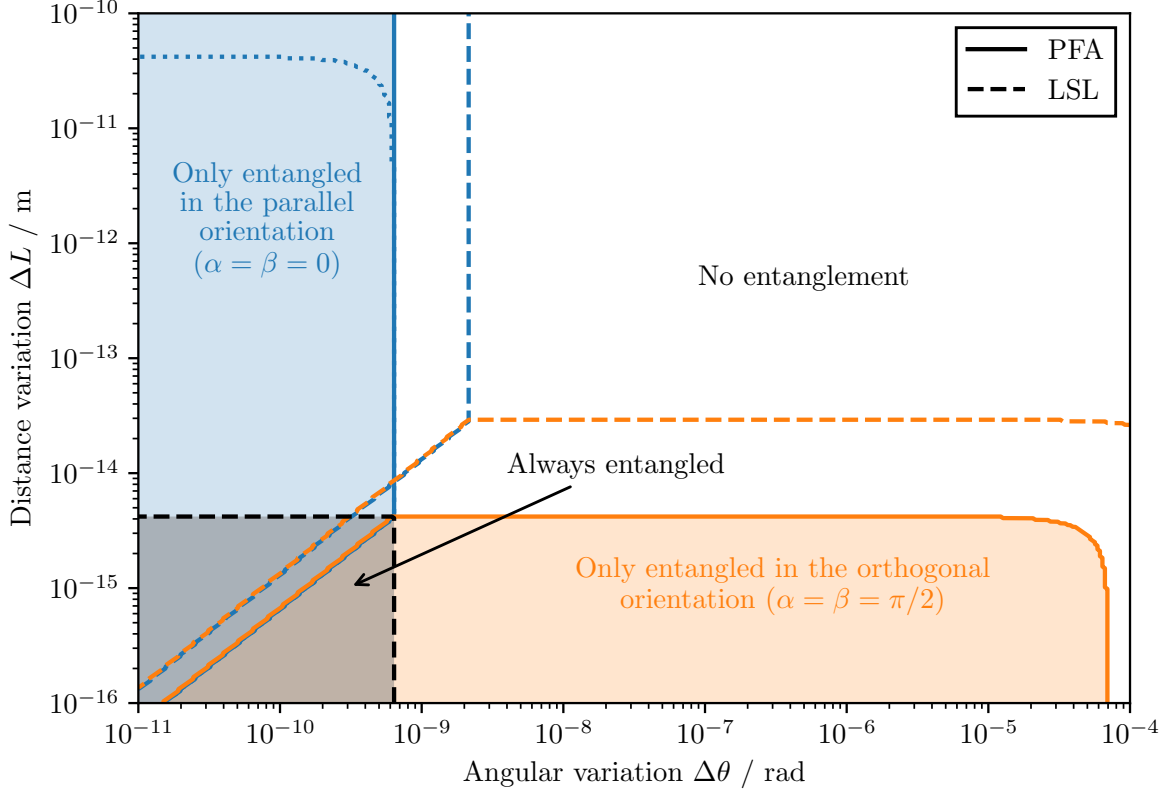


Figure 4.8: Optimal orientation for the experimental setup dependent on the variations in angle $\Delta\theta$ and distance ΔL for a initial separation distance of $L = 2R = 2 \times 10^{-5}$ m at time t_{\max} . The different predictions for the proximity-force-approximation (PFA) and the large-separation-limit (LSL) are shown. At a distance of $L = 20 \mu\text{m}$ the actual casimir interaction is somewhere in the middle between both approximations. In the region where entanglement is given regardless of the orientation (the bottom left), the orientation with *more* entanglement is still colored. The dotted line corresponds to the realistic upper bound discussed in the text.

4.2.2 Separation, mass and superposition size

It is possible to improve the required stability in placement and consequently the entanglement generation by changing the other parameters shown in fig. 4.1 besides the orientation. It is especially easy to modify the separation distance L during the experiment as one is only limited in the trap stability close to the shield discussed in section 4.3. The other parameters like the particle mass M and thus the radius R , the particle material and the superposition size Δx are considerably more difficult to change. One is limited by the experimental implementation of the spatial superpositions. Considering that up to date, the largest spatial superposition of a “macroscopic object” is in the order of $\Delta x \sim 500$ nm for masses of 4×10^{-23} kg [13], large changes in the delocalization size Δx or the particles mass might be virtually impossible. However, out of a theoretical standpoint, the effects of all these parameters and the improvements reachable in stability are interesting and considered in the following section.

Beginning with the effect of a larger particle-shield separation L , the improvements on angular stability are shown in fig. 4.9. A similar figure can be created for the stability of

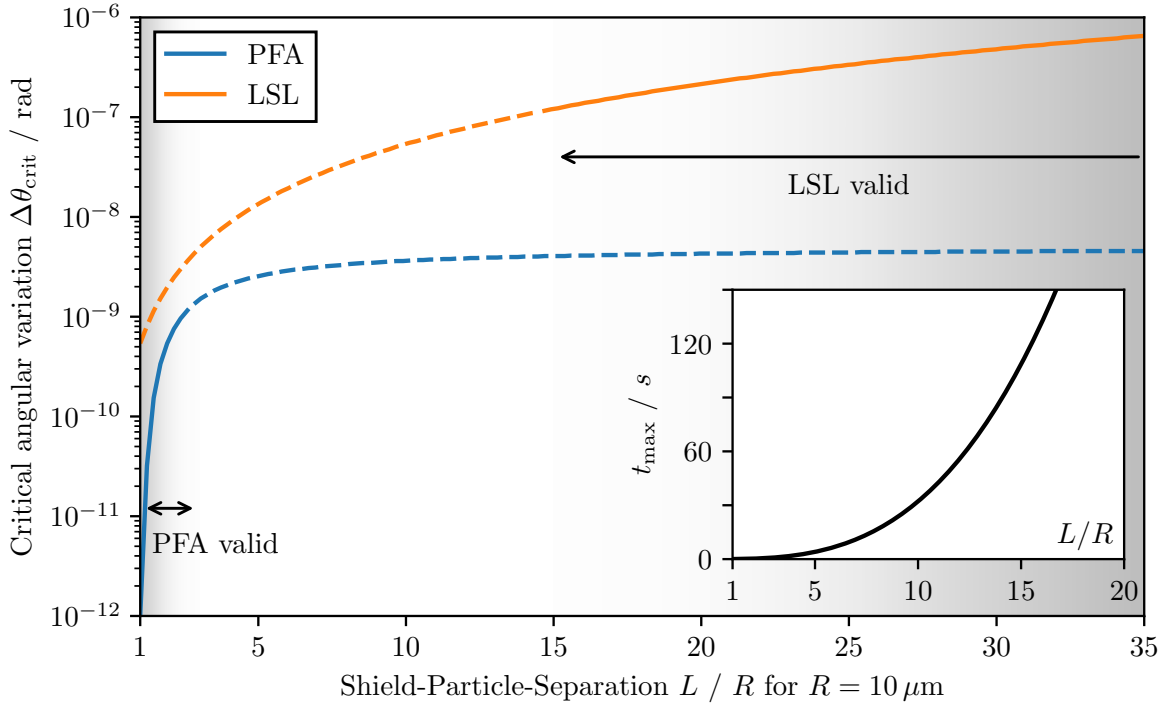


Figure 4.9: Stability against angular variations for increasing separation distances L in units of $R = 10 \mu\text{m}$ after a time $t_{\text{max}}(L)$. The dependence on the radius can be seen in fig. 4.10. Two models for the casimir-interaction are shown: The proximity-force-approximation (PFA) and the large-separation-limit (LSL). The regions outside the models validity are indicated with dashed lines. In the bottom right the time $t_{\text{max}}(L) \propto L^3$ is shown.

distance-variations ΔL , but as already discussed previously, the setup is very (infinitely) stable against small distance variations in the parallel configuration. It is intuitively clear that a larger separation improves the stability, as the relative effect of the variations $\sim \Delta x \sin \theta \ll L$ decreases and the Casimir potential tends towards zero. However, a larger separation also increases the time $t_{\max} \propto L^3$ until the maximum entanglement is built up. The combination of both effects leads to the result shown in fig. 4.9. Due to the strong distance dependence on the casimir model, both limits for either small separations $L \sim R$ (PFA) or large separations $L \gg R$ (LSL) have been compared. The “real” casimir potential lies somewhere between the two models. In general, it can be said, that a large separation is desirable, as long as the required coherence times are still reachable. Looking at the final averaged density matrix $\langle \rho \rangle$, it is possible to deduce the dependence of $\Delta\theta_{\text{crit}}$ on the separation L . The off-diagonal decoherence terms calculated in appendix D and given by eq. (D.8) scale similar to

$$\langle \rho_{ij} \rangle \sim \exp \left\{ - \left(\frac{2\phi_{\text{Casimir}}\Delta x}{(L - R - d/2)^3} \pm \frac{\phi_{\text{Gravity}}\Delta x}{4L^2} \right)^2 (\Delta\theta)^2 t^2 \right\} \quad (4.13)$$

where the gravity term can be neglected for small L ($\phi_{\text{Gravity}} \ll \phi_{\text{Casimir}}$). At the point $\Delta\theta_{\text{crit}}$ all entanglement is lost leading to $\langle \rho_{ij} \rangle \rightarrow 0$. The resulting dependence on ρ

$$\Delta\theta_{\text{crit}} \sim \frac{1}{t_{\max}} (L - R - d/2)^3 \sim \frac{(L - R - d/2)^3}{L^3} \quad (4.14)$$

which aligns very nicely with the blue curve for the PFA in fig. 4.9 ($R^2 = 0.99$). Similar arguments show that for large separations in the LSL the critical angular variation scales with $\Delta\theta_{\text{crit}} \sim L^2$.

The mass of the particles is determined by their radius R as well as their material. Most likely, the trapped and levitated particles are made of silica (SiO_2) with a density of $\rho_{\text{Silica}} = 2648 \text{ kg/m}^3$, as this material has been used widely in experiments on levitated nanoparticles [37, 38]. Due to its transparency, silica is very easy to trap in strong optical traps, but even quantum control in magnetic traps has been demonstrated with silica [38]. For this thesis, I will assume that all trapped particles are made of silica. Otherwise denser or heavier materials like e.g. stable osmium and lead isotopes would be worth considering. Trapping them in a paramagnetic trap could be theoretically possible and interesting as sufficient masses could already be reached with far fewer atoms and smaller particles, further improving coherence times and quantum control. The effect on angular stability of a larger and thus heavier particle is shown in fig. 4.10. It is important to note, that the time t_{\max} scales with M^{-2} and thus effectively with R^{-6} , making the effect of a slightly larger sphere very noticeable. One does need to find the ideal size of the sphere depending on what is possible experimentally: The mass must be large enough for gravity to have a measurable effect but simultaneously small enough for sufficient quantum control in the laboratory. Estimations suggest the usage of masses around the order of $10^{-11} \text{ kg} \approx 10^{-3} m_p$ as being possible [33]. The scaling of $\Delta\theta_{\text{crit}}$ with a changing size R of the particles can be determined similar to before. It

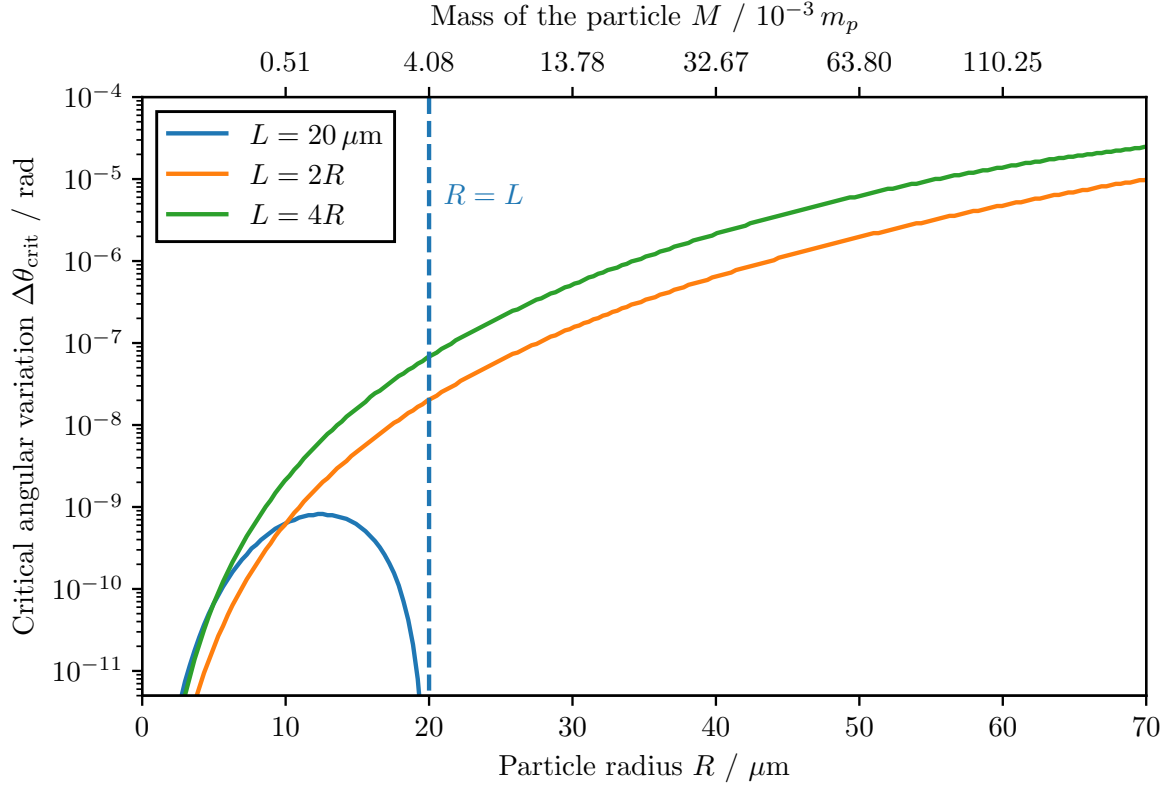


Figure 4.10: Critical angular variation $\Delta\theta_{\text{crit}}$ for different sized particles after a time $t_{\text{max}}(M)$. The mass of the corresponding particle in units of the Planck mass $m_p = \sqrt{\hbar c/G} \approx 2.176 \times 10^{-8} \text{ kg}$ is given on the top axis. For particles as large as the separation $R = L$, the surface-to-surface separation is almost zero, resulting in large casimir forces and thus no entanglement.

turns out, that for a constant separation L , the critical angular variation scales with

$$\Delta\theta_{\text{crit}} \sim \frac{(L - R - d/2)^3}{\phi_{\text{Casimir}}} \frac{1}{t_{\text{max}}} \sim \frac{(L - R - d/2)^3 R^6}{R} \quad (4.15)$$

whereas for $L \propto R$, the time $t_{\text{max}} \propto L^3/R^6$ varies additionally resulting in

$$\Delta\theta_{\text{crit}} \sim (R - d/2)^3 R^2. \quad (4.16)$$

The final parameter that theoretically be freely modified, is the size of the superposition Δx . A larger superposition size would increase the entanglement generation due to gravity because the differences in the distances between all superposition states would increase. Such effects ultimately lead to a faster build-up of entanglement scaling with $t_{\text{max}} \propto (\Delta x)^{-2}$. In matter wave experiments, superposition sizes of massive objects up to $\Delta x \approx 500 \text{ nm}$ were already achieved [13]. These sizes are much smaller than the size of the particle itself at $10 \mu\text{m}$. The effect of the superposition size on stability is shown in fig. 4.11. For large superposition sizes, the time until maximal entanglement

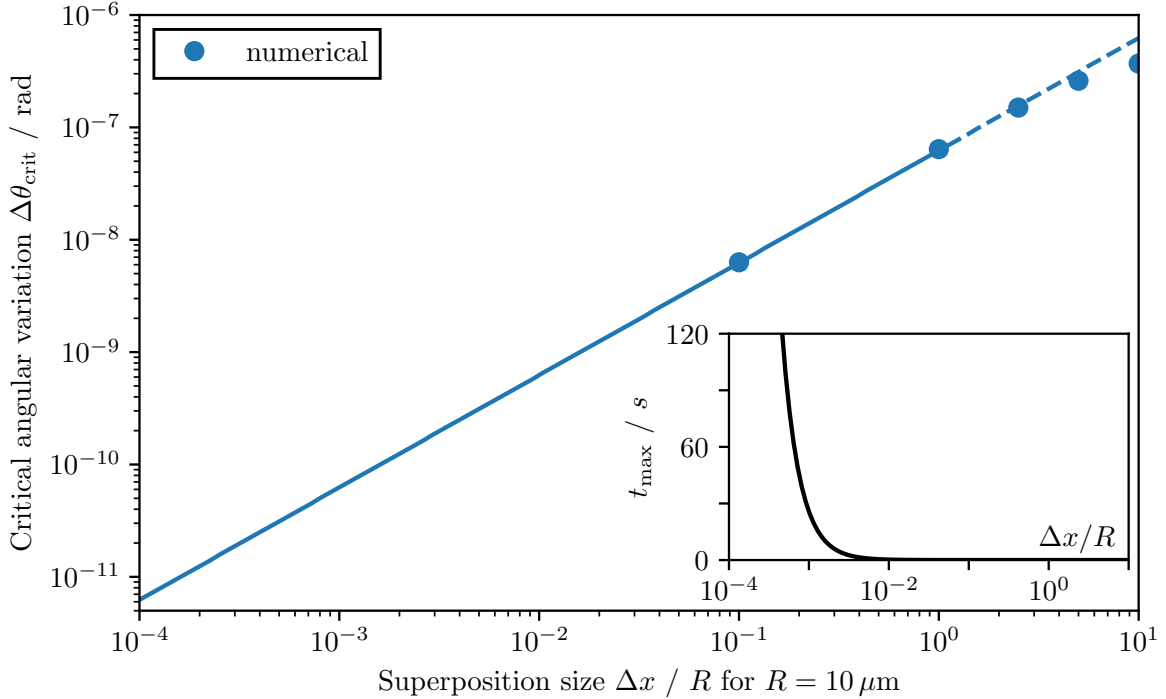


Figure 4.11: Effect of the superposition size Δx on the critical angular stability $\Delta\theta_{\text{crit}}$ after a time $t_{\text{max}}(\Delta x)$. For $\Delta x \gtrsim R$, numerical results are used. In the lower left, the time till maximum entanglement $t_{\text{max}} \propto (\Delta x)^{-2}$ is shown. For $\Delta x \ll R$, the resulting relation between Δx and $\Delta\theta_{\text{crit}}$ is linear.

is reached, decreases drastically. In the shorter time, the dephasing due to the casimir effect between the shield and the states is less substantial, increasing the stability against

variations in the placement. A larger superposition size on the other hand results in a greater effect of angular variations $\sim \Delta x \sin(\theta)$. Both of these effects result in a effective scaling of $\sim \Delta x$, which explains the linear curve¹⁰.

4.3 Trapping the particle

Another consequence of shielding that requires consideration is the trapping. Levitated particles are trapped and cooled in an ultra-high vacuum by either a magnetic, optical or electrical radiofrequency Paul-trap [39]. These traps differ in the trapping mechanism, but if the particle is cooled close to the ground state, all trapping potentials can be considered “harmonic” with trapping frequency $\omega_{\text{trap}} = 2\pi \times f$. The strength of the trapping potential $V \propto f^2$ differs for the different trapping types. Typical values range from 1 Hz – 1 kHz for magnetic traps [38, 39] up to 10 kHz – 300 kHz for optical traps [39]. The different types of traps also offer different advantages and disadvantages: Optical traps are relatively noisy due to the constant interaction between the particle and the light. Magnetic traps for large particles are less noisy, but only low trapping frequencies are possible [39]. For electric traps, the particle must be charged, which causes a lot of different problems, as seen in section 5.1.

If the particle in the harmonic trapping potential is placed close to the shield, the Casimir interaction $\sim \mathcal{L}^{-2}$ can disturb the trapping and eventually even suck the particle onto the shield. The total potential $V_{\text{tot}} = V_{\text{trap}} + V_{\text{Casimir}}$ is shown in fig. 4.12 for a stable and unstable configuration. Due to the influence of the attractive Casimir force, the equilibrium position of the trap shifts slightly closer to the shield by $\Delta\xi$. This shift

$$\Delta\xi = \frac{-\nabla V_{\text{Casimir}}}{m(2\pi f)^2} = \frac{2\hbar c\pi^3}{720} \left(\frac{\varepsilon_r - 1}{\varepsilon_r + 1} \right) \varphi(\varepsilon_r) \frac{R}{\mathcal{L}^3} \frac{1}{m(2\pi f)^2} \quad (4.17)$$

is negligibly small as it is in the order of $\Delta\xi \approx 10^{-13}$ m for $f = 1$ kHz and $L = 2R = 20 \mu\text{m}$.

To determine the stability of a trapped particle with mass $M \propto R^3$ in a trap with frequency f placed at a distance $L_0 > R$ in front of the shield, the number of bound energy-eigenstates in the potential V_{tot} is considered. From fig. 4.12 it becomes clear, that as long as the particles thermal energy is well below E_0 , the trap is stable and the particle is bound. Here, E_0 is defined as the local maximum of the potential

$$E_0 = \max_{L \in (R, L_0)} (V_{\text{trap}} + V_{\text{Casimir}}) \quad (4.18)$$

where L_0 is the position where the particle is trapped. If there does not exist a local maximum, i.e.

$$\frac{\partial}{\partial L} (V_{\text{trap}} + V_{\text{Casimir}}) > 0 \quad (4.19)$$

¹⁰Here it is shown in a double-logarithmic plot. The relation between Δx and $\Delta\theta_{\text{crit}}$ is nevertheless linear, which can be seen with similar arguments as used previously.

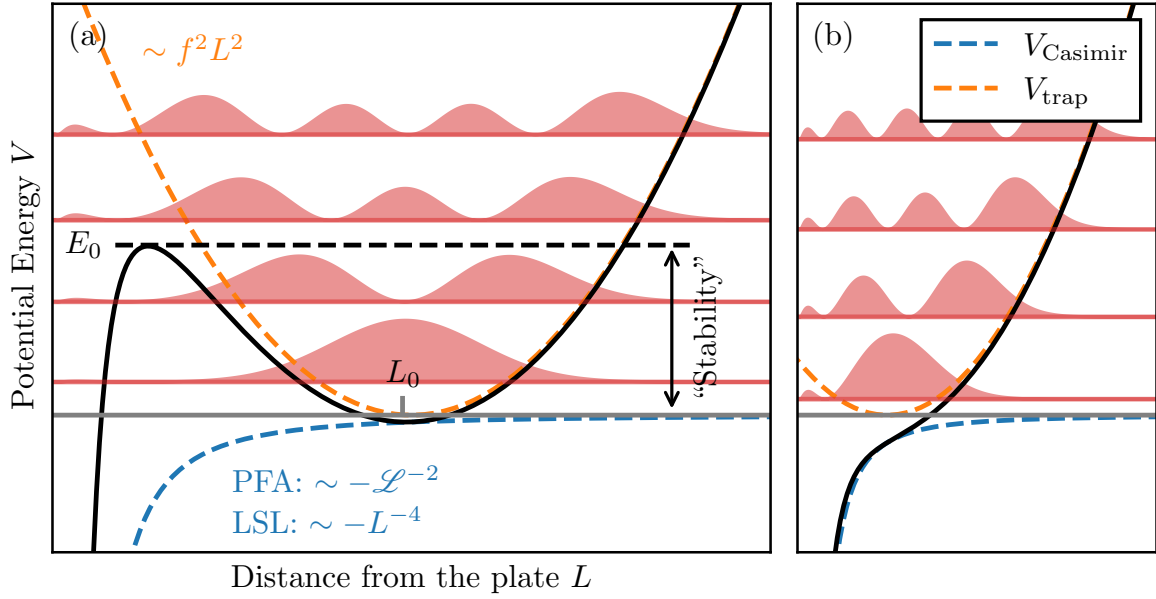


Figure 4.12: Visualization of the potential as an overlay of the harmonic trapping potential $V_{\text{trap}} = m(2\pi f)^2 L^2/2$ and the casimir potential V_{Casimir} . f is the trapping frequency and L_0 the position of the trap. In red, eigenstates of the potential are visualized offset by the eigen-energies. **(a)** Almost harmonic bounded potential which can hold the particle, if its energy is less than E_0 . **(b)** Potential with no bounded states. Here, trapping is not possible.

for all $L \in (R, L_0)$, the resulting trap cannot be stable. These regions of no stability are shown as a white area in the stability diagram fig. 4.13. In the general case, the stability can be measured by computing the number of bound eigenstates $n(E_0)$ with energies less than E_0 and comparing them with the number of thermally excited states \bar{n} . At a temperature T on average

$$\bar{n} = \frac{1}{e^{\beta\hbar\omega} - 1} \quad (4.20)$$

states are occupied, where $\beta = 1/k_B T$ and $\omega = 2\pi f$. This is true, as long as the potential is assumed to be harmonic, which is, as seen shortly, a very good approximation. To find the number of possible bound energy-eigenstates in the potential, I am using the **WKB-approximation** [40]. In this approximation, the energy of the n -th eigenstate of a smooth and appropriately slow varying potential $V(x)$ can be calculated using [40, p. 163]

$$\int_{x_1}^{x_2} dx \sqrt{2m(E - V(x))} = \left(n + \frac{1}{2}\right) \pi \hbar, \quad (4.21)$$

where $V(x_1) = V(x_2) = E$ are two turning points corresponding to energy E . Conversely, it is possible to use this approximation to numerically estimate the total number of bound states in the potential $V = V_{\text{trap}} + V_{\text{Casimir}}$ using

$$n(E_0) \approx \frac{1}{\hbar\pi} \int_{x_1}^{x_2} dx \sqrt{2m(E_0 - V(x))}, \quad (4.22)$$

which is closely given (highest deviation around 40%; averaged relative error $\sim 0.9\%$) by the harmonic approximation $n(E_0) \sim E_0/\hbar\omega$. The resulting number of bound states is shown in fig. 4.13 as well as the stability boundaries at specific temperatures where $\bar{n} = n(E_0)$. It turns out, that regardless the type of the trap, a successful trapping even at room temperature should be possible as long as the particle is placed appropriately far away from the trap. The ability to trap and levitate the masses is therefore not significantly impaired by the presence of the Faraday shield.

4.4 Discussions

Looking at the preceding results, it is clear that the planned experiment represents a significant engineering challenge. The decoherence due to the Casimir interactions between the particles and the Faraday shield requires a accuracy in the placement of the particles in the order of $\Delta L = 10^{-10}$ m and $\Delta\theta = 10^{-9}$ rad. Achieving these accuracies appears to be very challenging and it will be necessary to adjust the originally proposed parameters in fig. 4.1. The separation distance L as well as the orientation are particularly easy to change. As discussed earlier, the parallel orientation might be the only viable option, as this position is almost infinitely stable against variations in the distance. The orthogonal orientation would require placement accuracies in the order of single atoms (compare to fig. 4.7). The separation L can be freely chosen and a larger separation reduces the effect of placement variations as seen in fig. 4.9 but substantially

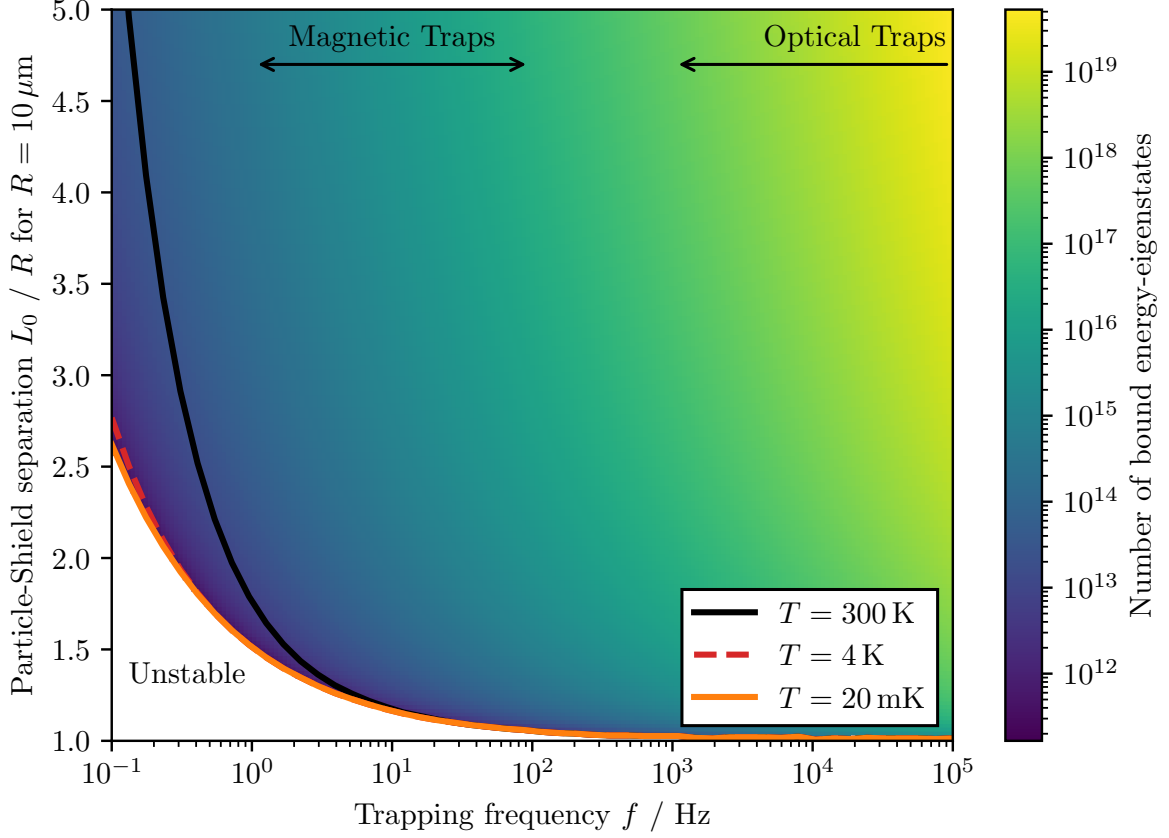


Figure 4.13: Stability diagram for different trapping frequencies $f = \omega/2\pi$ and particle-shield separations L_0 . The number of bound energy-eigenstates for each combination of f and L_0 are calculated using the WKB-approximation. The number of thermally occupied states \bar{n} at different Temperatures is overlaid. As an example, for $f = 1$ Hz, $\bar{n}(T = 300 \text{ K}) \approx 10^{13}$ states are thermally occupied. All regions below these boundaries are unstable. A increase in the radius R and thus the mass M improves the regions of stability massively.

increases the required coherence time $t_{\max} \propto L^3$. It could also be argued that at a distance of $L \geq 200 \mu\text{m} = 20R$ (compare to section 2.3), the Faraday shield would no longer be required because the Casimir forces between the particles are 10 times weaker than the gravitational interactions due to their rapid decrease at large distances ~ 10 . However, the loss of entanglement due to angular and distance variations in placement is not solely due to Casimir forces between the particle and the shield, so that a complete removal of the shield does not fully eliminate the requiem placement accuracy. The slightly varying gravitational interaction alone can induce enough decoherence on its own to destroy entanglement. The critical variations for a gravitational interaction alone in the parallel configuration after t_{\max} are given by $\Delta\theta_{\text{crit, ideal}} = 1.1 \times 10^{-3}$ rad and $\Delta L_{\text{crit, ideal}} = 7 \times 10^{-4}$ m, which should not pose an engineering problem.

Changing the other parameters such as the particles size or superposition size might not be possible. Substantially changing both would increase the difficulty in groundstate cooling and quantum control unforeseeable. For all these considerations, the trapping does not play a role as this should be possible with a suitable magnetic or optical trap for almost any possible configuration of the setup parameters (compare to the results from section 4.3).

One of the objectives of this thesis is, to determine whether it is possible to bring the particles closer together through the presence of the Faraday shield in order to increase gravitational entanglement and reduce the required coherence times. To achieve this, the previous results from this chapter can be used find the optimal parameters of the experimental setup. The goal of the optimization process can be expressed as the following: One wants to get *as much entanglement as possible* in the *shortest time possible* with the *largest possible variations* in the placement while still considering the limitations in the mass as well as in the superposition size.

In full generality, it is not possible to find a local optimum for choosing the parameters. This is because (if the mass M and the superposition size Δx is fixed) the coherence time - which should be minimized - scales with $t \propto L^3$ by eq. (4.10) and the critical angular variation - which should be as large as possible - scale with $\Delta\theta_{\text{crit}} \propto (L - R)^3/L^3$ for small separations (eq. (4.14)) or $\Delta\theta_{\text{crit}} \propto L^2$ for $L \gg R$. Both of these optimization criteria cannot be fulfilled simultaneously as long as no constraints are given. Given however a coherence time t_{target} and/or the minimum possible placement accuracy, it is possible to determine the required sphere-plate separation L as well as the amount of entanglement, one can maximally expect using the following steps:

1. Lets assume that the size of the particle R and consequently the mass $M = 4/3\pi R^3 \rho_{\text{Silica}}$ as well as the superposition size Δx are fixed. An increase in either of them would have a positive effect of the optimization goal stated above, as the time t_{\max} decreases and the stability against placement variations increases simultaneously.

2. The following ratio given by eq. (4.10) and by Ref. [33] to

$$\frac{M^2(\Delta x)^2}{L^3} t_{\max} = \frac{8\pi\hbar}{G} = \text{const.} \quad (4.23)$$

in the parallel orientation is fixed. For orthogonal configurations, this constant would reduce by a factor of $1/2$.

3. In general it is possible to measure at a earlier time $t_{\text{target}} = \tau t_{\max}$ (i.e. the coherence time) with $\tau \leq 1$, where less total entanglement has been build up but in general a grater stability against placement variations can be achieved (see fig. 4.3). Putting all assumptions together, the ratio

$$\frac{t_{\text{target}}}{\tau L^3} = \frac{8\pi\hbar}{G} \frac{1}{M^2(\Delta x)^2} \quad (4.24)$$

is constant.

4. In the parallel orientation, the distance variations don't matter as the system is infinitely stable against variations in the particle-shield separation. The critical angular variation however scales like $\Delta\theta_{\text{crit}} \sim (L - R)^3/L^3$ for small distances and like $\Delta\theta_{\text{crit}} \sim L^2$ shown in fig. 4.9. it is therefore possible to determine the minimum separation $L_{\min} > R$ for a given placement accuracy.
5. Using the required separation, one can calculate $\tau \in (0, 1]$ using eq. (4.24) and look up the maximal possible entanglement in the top right of fig. 4.3 after an evolution time τt_{\max} .

As an example, the radius is fixed as $R = 10\mu\text{m}$ and the superposition size is $\Delta x = 100\text{nm}$. Such a particle can be placed with an accuracy of $\Delta\theta = 10^{-7}\text{rad}$ and coherence times of 1 s are reachable. Using the steps outlined above, the resulting particle-shield separation is around $L \approx 15R$ and the maximal amount of measurable entanglement is given by $E_N \approx 9.2 \times 10^{-3}$. For more entanglement, either a heavier particle, a larger superposition size, a higher placement accuracy or larger coherence times are required. It is therefore actually possible, to bring the particles closer together than without the Faraday shield and still measure entanglement. One is only limited by the placement accuracy and repeatability.

5 The consequences of a thermal shield

Why a shield, what does the shield do, maybe short introduction

- Small shield maybe better
- Difference between small and large shield
- Small shield: Take maximum (or minimum) and this is the casimir force. This is the same as just a angle $\Delta\theta$
- Large shield: $\Delta\theta$ and ΔL
- Use linearity of arctan and central-limit-theorem: This angle is the same as always above
- Entanglement generated by the shield
- Entanglement dynamics with extra shield vibrations

5.1 Thickness and size of the shield

The thickness and size of the shield can be estimated by considering a real material. The shield material should have a large electric conductivity σ and should therefore behave like an conductor. Even a superconducting shield could be considered. For a real metal like for example copper, the transmission T of electromagnetic waves is given by [41]

$$T = \left| \frac{\mathbf{E}_{\text{after}}}{\mathbf{E}_{\text{before}}} \right| = \frac{2}{Z_0 \sigma d} \quad (5.1)$$

where σ is the electric conductivity, $Z_0 = 377 \Omega$ the impedance of free space (provided the shield is placed in a vacuum or air) and d the thickness of the shield. The electric conductivity has a strong dependence on temperature and decreases with $1/T^5$ ¹¹ with increasing temperatures [43, p. 284-286]. The electric conductivity for copper at room temperature ($\sigma = 59.6 \times 10^6 \text{ S/m}$) should therefore be a very valid worst-case approximation. Measured data suggest a conductivity of $\sigma(T = 10) \approx 1.5 \times 10^{10} \text{ S/m}$ [42].

¹¹This behavior is only true for temperatures below the Debye temperature. For copper, this limit is around $\Theta_D = 343 \text{ K}$. In the experiment, the shield is cooled down, so the low-temperature limit of the electric conductivity for metals is very valid [42].

In general should the thickness of the shield be chosen as thin as possible. Otherwise, the distance between the masses has to increase accordingly and the gravitational potential between them gets smaller. This would require longer coherence times till a sufficient amount of entanglement could be measured. To estimate the thickness of the shield, I am using the condition, that entanglement between the masses should be built up mainly due to gravity. All other possible interactions like Coulomb or Casimir forces, should be suppressed sufficiently by the shield. To quantify the amount of entanglement built-up over time, I obt for a measure called **entanglement rate**

$$\Gamma = \left. \frac{d}{dt} E_N(\rho) \right|_{t=0} \quad (5.2)$$

where E_N is an appropriate entanglement measure - in this case the logarithmic negativity from section 2.2. For the gravitational entanglement, this can be calculated by eq. (2.23) and for the parallel configuration this is given by

$$\Gamma_{\text{Gravity}} = \frac{GM_A M_B (\Delta x)^2}{16\hbar L^3 \log 2}. \quad (5.3)$$

The entanglement rate for other interactions should be smaller (and ideally a lot smaller) than the entanglement rate due to gravity. In the following, this is considered for Coulomb- and Casimir interactions.

5.1.1 Shielding Coulomb-Interactions

The main focus of the shield is to block electromagnetic interactions between the spheres. Experimentally, it might be beneficial for the spheres to carry a small amount of charge to help with the trapping. !!!CITATIONS!!! The Coulomb interaction potential energy

$$V = \frac{1}{4\pi\epsilon_0} \frac{q_A q_B}{2L} \quad (5.4)$$

between the spheres has the same structure as the gravitational potential and can therefore induce entanglement by the same logic. Using a shield, this coupling is suppressed by a factor of T . The entanglement rate Γ_{Coulomb} is therefore easily calculable in a similar form as eq. (5.3) to

$$\Gamma_{\text{Coulomb}} = \frac{T |q_A q_B| (\Delta x)^2}{64\pi\epsilon_0 \hbar L^3 \log 2} \quad (5.5)$$

Requiring that $\Gamma_{\text{Gravity}} > \Gamma_{\text{Coulomb}}$, this inequality yields a maximum transmission and thus a minimum thickness of

$$T \frac{|q_A q_B|}{4\pi\epsilon_0} < GM_A M_B \quad (5.6)$$

$$\Longleftrightarrow d > \frac{1}{2\pi\epsilon_0 Z_0 \sigma G} \frac{|q_A q_B|}{M_A M_B} = \frac{9}{32} \frac{1}{Z_0 \sigma} \frac{1}{\pi^3 \epsilon_0 G \rho^2} \frac{e^2}{R^6} \quad (5.7)$$

where in the last step $M_A = M_B$ and $q_A = q_B = e$ has been assumed. The shield thickness heavily depends on the radius of the spheres where small and light masses make the shield unworkably thick. A silica sphere with a radius of $R = 10^{-5}$ m would require a shield around the thickness of 10 nm at 4 K up to $2.5 \mu\text{m}$ at room temperature. A realistic thickness for the shield at low temperatures could therefore be $d = 100$ nm.

Electric fields however can still propagate around a Faraday shield of finite size and induce entanglement. It is however possible, to estimate the required radius r_s of the shield to block a specific amount η of the electric field. The resulting radius corresponding to η is derived in appendix C.1 and the result is shown in fig. 5.1. The transmission

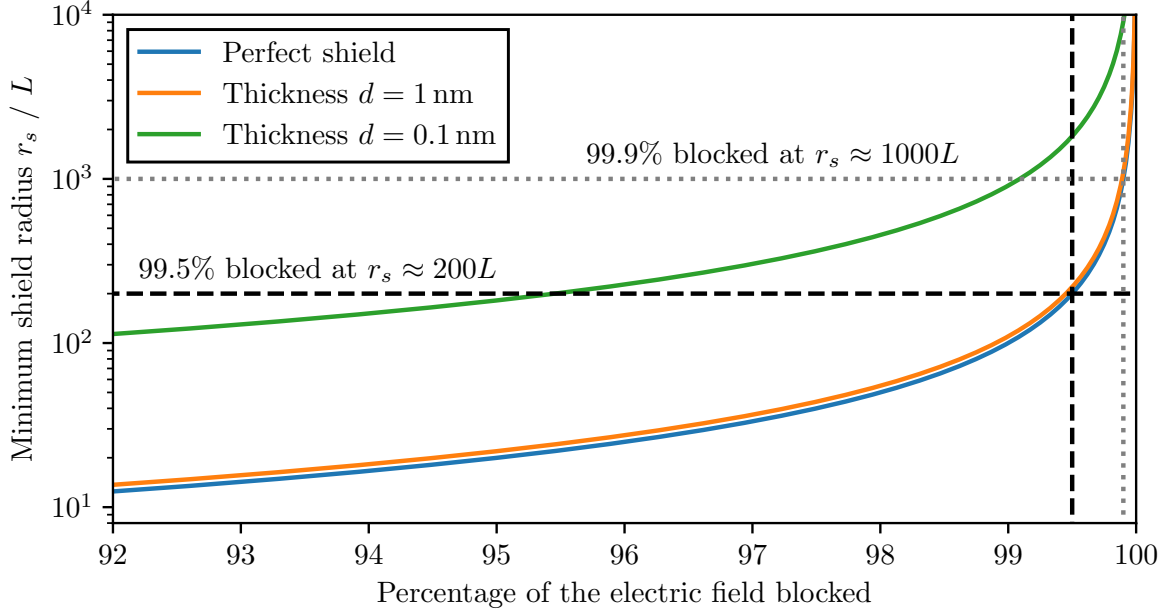


Figure 5.1: Radius of the shield depending on the shield effectiveness η . Additionally a real shield with different thicknesses d at room temperature is considered. For a shielding between 99.5...99.9% ($\eta = 0.995...0.999$), a radius of at least $r_s = 200...1000L$ should be used. For a sphere-plate distance of $L = 2 \times 10^{-5}$ m, the shield radius should be in the order of millimeters and centimeters.

T should be replaced by a modified transmission $\tilde{T} = T\eta + (1 - \eta)$ where the shield effectiveness η depends on r_s . Now, the condition eq. (5.6) introduces a limit for the minimum effectiveness and thus a limit on the minimum radius of

$$\eta_{\min} = 1 - \frac{4\pi\epsilon_0 GM_A M_B}{|q_1 q_2|}. \quad (5.8)$$

Thus using the setup with the parameters from earlier, a minimum effectiveness of $\eta_{\min} \gtrsim 0.99997$ and thus a radius of $\gtrsim 66$ cm is required. This shield is too large for all practical purposes and it might be beneficial to choose slightly heavier masses to

reduce the shield size to the orders of ~ 1 cm. This would require both spheres to have approximately double the radius than before. Using neutral masses without any charge would be also beneficial and the shield size could be reduced to only the size of the spheres themselves, however it might be an engineering challenge, to trap and levitate uncharged massive particles.

5.1.2 Shielding Casimir-Interactions

Similarly to Coulomb interactions, it is possible to estimate the required thickness of the shield necessary to sufficiently suppress Casimir interactions. Between two spheres with radius R and separation $2L$, the Casimir potential reads [21]

$$V = -\frac{23\hbar c}{4\pi \cdot 128L^7} \left(\frac{\varepsilon_r - 1}{\varepsilon_r + 2}\right)^2 R^6. \quad (5.9)$$

The entanglement rate can be obtained similarly as before by expanding the casimir potential between the spheres in small Δx and computing the logarithmic negativity as before:

$$\Gamma_{\text{Casimir}} = T^2 \frac{161}{4096} \frac{cR^6(\Delta x)^2}{\pi L^9 \log 2} \left(\frac{\varepsilon_r - 1}{\varepsilon_r + 2}\right)^2. \quad (5.10)$$

The dependence on T^2 is only a systematic guess but should be sufficient for a basic estimation. Casimir and van der Waals forces are second order effects in the dipole-dipole interaction [23]. Demanding again, that the entanglement due to gravity should be mediated faster than due to Casimir interactions $\Gamma_{\text{Gravity}} > \Gamma_{\text{Casimir}}$, one arrives at the expression

$$T^2 \frac{161cR^6}{256\pi L^6} \left(\frac{\varepsilon_r - 1}{\varepsilon_r + 2}\right)^2 < \frac{GM_A M_B}{\hbar} \quad (5.11)$$

$$\iff d^2 > \frac{4 \cdot 161c\hbar R^6}{256Z_0^2\sigma^2\pi L^6 GM_A M_B} \left(\frac{\varepsilon_r - 1}{\varepsilon_r + 2}\right)^2 \quad (5.12)$$

$$\iff d > \sqrt{\frac{1449}{4096} \frac{c\hbar}{G\pi^3} \frac{2}{Z_0\sigma\rho L^3} \frac{\varepsilon_r - 1}{\varepsilon_r + 2}} \quad (5.13)$$

where again in the last step I assume $M_A = M_B$. For large separations, the shield thickness can go arbitrary low because of the weakness of the casimir interactions at larger distances. Between two silica spheres separated in the order of magnitude as the radius ($L = 2 \times 10^{-5}$ m), the required minimum thickness is between 4×10^{-11} m at 4 K and 10 nm at room temperature. Either way, it is much thinner than a Faraday shield required to shield electrostatic Coulomb interactions. The effect of ε_r was neglected in these numbers. The minimum thickness only changes by a factor between 0...1 due to dielectric materials. In fact, these thicknesses are much thinner than recommended, because the shield loses rigidity. It turns out that the vibrational frequency depends linearly on the thickness and thus more vibrations are possible. A more detailed discussion of this matter is given in the next section.

5.1.3 Gravitational effects of the shield

For simplicity, in the following estimations of the attractive gravitational force between an infinitely large plate with thickness d and a sphere positioned a distance L in front of the plate is calculated. This should slightly overestimate the actual force due to a finite plate¹². The gravitational force between the sphere and a infinitesimal mass segment $dm = r\rho d\varphi dr$ of the plate with density ρ at a distance r from the center is given by

$$d\mathbf{F} = \frac{GMdm}{\ell^2} \hat{\ell} \Rightarrow dF_z = \frac{GM\rho d}{\ell^2} dr d\varphi \cos \theta, \quad (5.14)$$

where $\ell^2 = r^2 + L^2$ denotes the distance between the sphere and the mass segment and $\theta = \arccos L/\ell$ is the angle between them. The total force between the sphere and the infinite plate is therefore given by

$$F_z = GM\rho dL \int_0^\infty dr \int_0^{2\pi} d\varphi \frac{r}{(r^2 + L^2)^{3/2}} = 2\pi GM\rho d. \quad (5.15)$$

This result is independent of the distance L and a numerical value for a copper shield ($\rho = 8960 \text{ kg/m}^3$) with thickness of $d = 100 \text{ nm}$ and the silica sphere already used in chapter 2 is given by $F \approx 4.2 \times 10^{-24} \text{ N}$. Compared with the attractive force between two silica spheres separated by a distance of $2L = 4 \times 10^{-5} \text{ m}$, the force due to the plates is smaller by a factor of ≈ 0.8 . Both forces are therefore comparable and the thickness of the shield should be chosen as thin as possible to not influence the gravitational sensing of the masses. If the shield is not perfectly placed in the center between the two masses or if the shield is uneven due to e.g. thermal vibrations, these gravitational effects might be able to destroy entanglement by inducing non-global phases to the cat-states.

5.2 Thermal shield vibrations

A spherical plate that is fixed at the edge can vibrate in different vibrational modes labeled by the indices (k, l) where $k \in [1, \infty)$ and $l \in [0, \infty)$. The exact vibrational frequency and the mode shape can only be given in terms of the Bessel functions. In fact, one of the first occurrences of these functions can be traced back to Euler trying to solve the very similar problem of a vibrating perfectly flexible membrane [44]. In general, the vibrations of a plate with thickness d can be described by the differential equation [45, p. 490]

$$D\nabla^2 \nabla^2 u = -\rho d \ddot{u} \quad (5.16)$$

where D is given by material properties like Youngs module E and the poisson number ν as

$$D = \frac{d^3 E}{12(1 - \nu^2)}. \quad (5.17)$$

¹²In fact, using a finite shield with radius $r_s = 0.01 \text{ m}$, the total force decreases only by 0.2% compared to an infinitely sized one.

The general solution of this differential equation can be written in terms of the Bessel functions as (derived in Ref. [45, p. 490-495])

$$u_{kl}(r, \theta, t) = z \left[J_l(\beta_k r) - \frac{J_l(\beta_k r_s)}{I_l(\beta_k r_s)} I_l(\beta_k r) \right] \cos(l\theta + \phi_1) \sin(\omega_{kl}t + \phi_2) \quad (5.18)$$

with

$$\beta_k = \frac{\tilde{r}_k}{r_s} \quad \text{and} \quad \omega_{kl} = \frac{\tilde{r}_k^2}{r_s^2} \sqrt{\frac{D}{\rho d}} = \tilde{r}_k^2 \frac{d}{r_s^2} \sqrt{\frac{E}{12\rho(1-\nu^2)}}, \quad (5.19)$$

where \tilde{r}_k is the k -th solution of the equation

$$J_l(\tilde{r}_k)I_{l+1}(\tilde{r}_k) + I_l(\tilde{r}_k)J_{l+1}(\tilde{r}_k) = 0. \quad (5.20)$$

The phases ϕ_1 and ϕ_2 can be determined by initial conditions and refer to the rotation of the plate as well as temporal offsets. The first few modes are shown in fig. 5.2. In general, every possible vibration of the plates can be expressed as a sum of these default modes u_{kl} . The amplitude z of the vibrations are determined by the thermal temperature and can be estimated by treating the amplitude of each vibration as a quantum harmonic oscillator with frequency ω_{kl} . The expectation value of the amplitude $\langle \hat{z} \rangle$ is obviously zero and the variance $(\Delta \hat{z})^2 = \langle \hat{z}^2 \rangle - \langle \hat{z} \rangle^2$ at temperature T is given by

$$(\Delta \hat{z}_{kl})_T^2 = \frac{\hbar}{2\tilde{m}\omega_{kl}} \coth\left(\frac{\hbar\omega_{kl}}{2k_B T}\right) \approx \frac{k_B T}{\tilde{m}\omega_{kl}^2} \quad (5.21)$$

A derivation of this is given in appendix C.2. In the last step $\hbar\omega \ll k_B T$ was used. \tilde{m} is the *effective mass* of the mode in which the precise shape is considered. A intuitive estimation for this mass can be given by the average of the mode

$$\tilde{m} = m \frac{1}{\pi r_s^2} \int_0^{r_s} dr \int_0^{2\pi} r d\theta u_{kl}(r, \theta, t). \quad (5.22)$$

with $m = \rho\pi r_s^2 d$ being the total mass of the shield.

5.2.1 Occupation of the vibrational modes

$$\hat{H} = \hbar\omega \left(\hat{a}^\dagger \hat{a} + \frac{1}{2} \right) + \tilde{g}_A(\hat{z}) |\psi_A\rangle\langle\psi_A| + \tilde{g}_B(\hat{z}) |\psi_B\rangle\langle\psi_B| \quad (5.23)$$

Solution:

$$\rho(t) = \frac{1}{2} \begin{pmatrix} 1 & e^{-i\varphi(t)} e^{-\gamma(t)} \\ e^{i\varphi(t)} e^{-\gamma(t)} & 1 \end{pmatrix} \quad (5.24)$$

with the phase

$$\varphi(t) = \frac{1}{\hbar^2 \omega^2} (\sin(\omega t) - \omega t) (g_A^2 - g_B^2) \quad (5.25)$$

and the decoherence term

$$\gamma(t) = \frac{4(g_A - g_B)^2}{\hbar^2 \omega^2} \sin^2\left(\frac{\omega t}{2}\right) \left[\bar{n} + \frac{1}{2} \right] \quad (5.26)$$

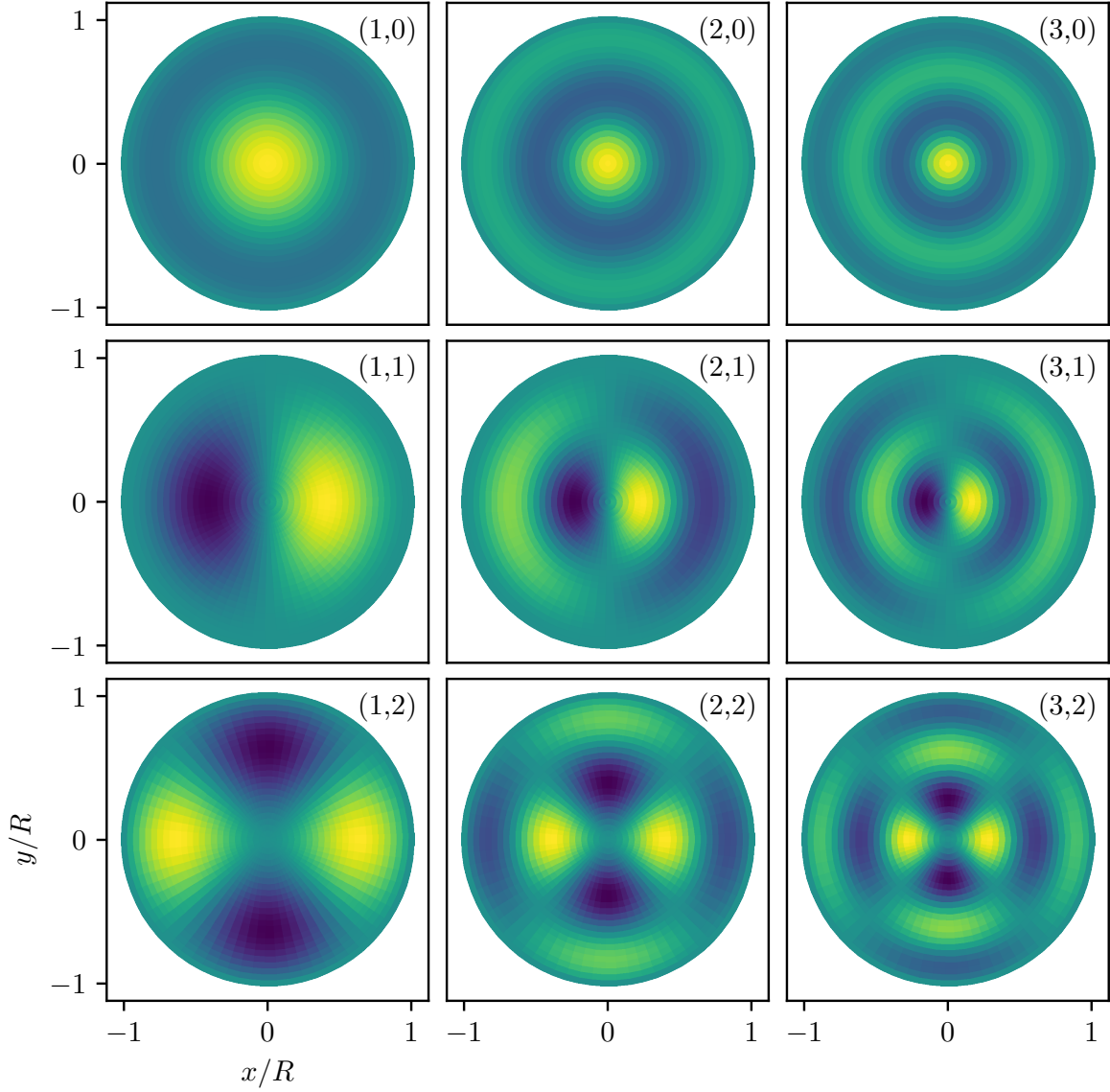


Figure 5.2: Normalized shape of the vibrational modes (k,l) of a vibrating spherical plate fixed at the edge with $R/d = 1000$.

5.3 Discussions on the shield

- ****Charged or uncharged**** Compare requirements in size and thickness as well as thermal vibrations, which are less a problem for smaller shields
- Small shield = local casimir effect. Compare with sec. 3.3
- How large are the effects of thermal vibration and how bad is everything (Maybe in the next section, otherwise a little bit chaotic)

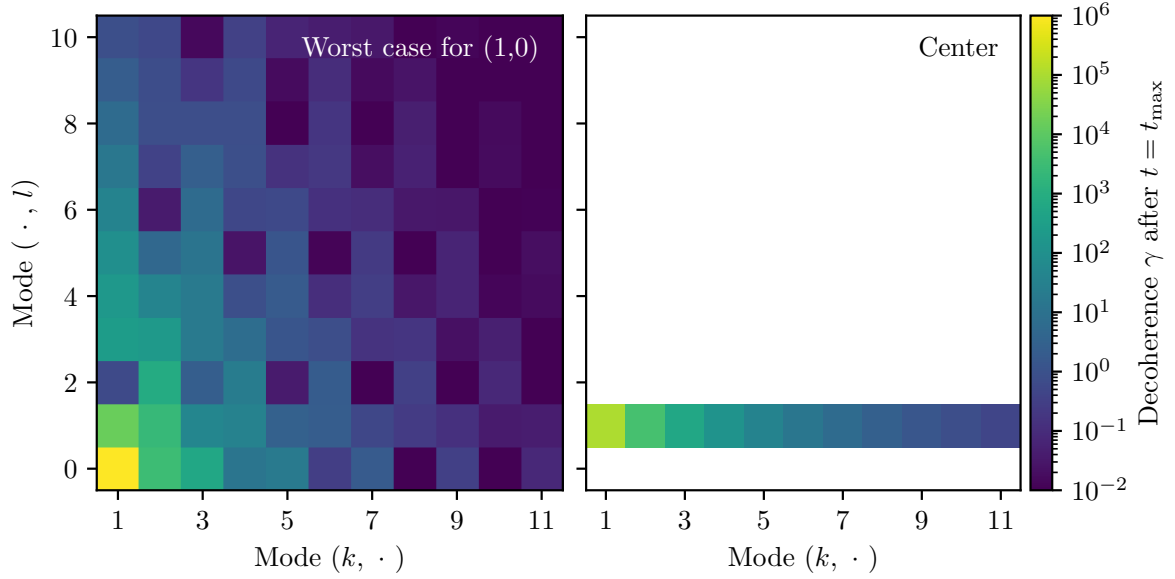


Figure 5.3: Maximum decoherence γ at 4 K for all modes if the cat-state is placed **left:** at the point with maximum gradient of the mode (1,0) and **right:** in the center of the plate. It becomes evident, that only a few low modes play an actual role for the total dephasing.

- Maybe a cross-structure or a different geometry of the shield could reduce vibrations and a larger shield might be okay. But local structures again
- Rectangular plate (frequencies only one order of magnitude ($\sqrt{\pi^4}$) better -i no real improvements)
- Possible to measure casimir forces with a similar technique of dephasing (very sensitive)

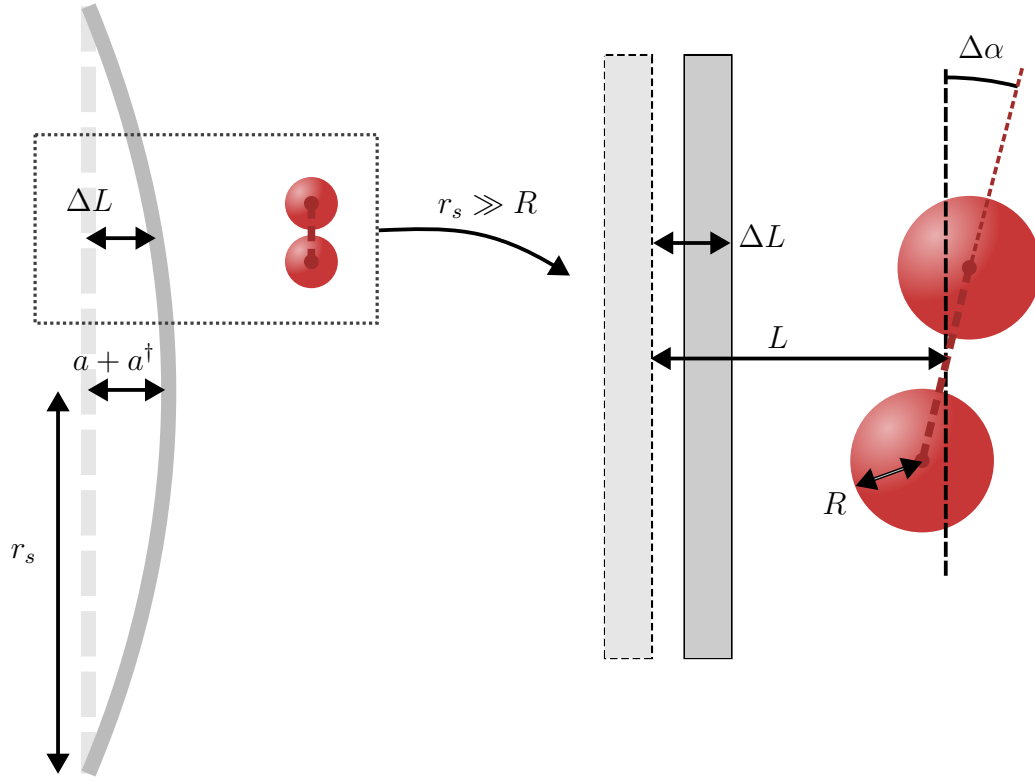


Figure 5.4: For a large shield, vibrations can be interpreted locally as if one mass was a distance ΔL further away from a shield and the other one ΔL closer and as if both masses would be rotated by an angle $\Delta\theta$.

Table 5.1: large shield ($r_s \gg R$) and a small shield in the size of the particle size $r_s \sim R$. At 4 K.

Modes (k, l)	large shield ($r_s \gg R$)				small shield
	Maximum gradient		Center ^a		$\Delta\theta/\text{rad}$
	$\Delta\theta/\text{rad}$	$\Delta L/\text{m}$	$\Delta\theta/\text{rad}$	$\Delta L/\text{m}$	
(1, 0)	3.0×10^{-7}	9.3×10^{-10}	-	1.9×10^{-9}	1.9×10^{-7}
(1, 1)	7.8×10^{-8}	4.8×10^{-10}	2.1×10^{-7}	-	1.3×10^{-7}
(2, 0)	6.6×10^{-8}	1.7×10^{-10}	-	4.7×10^{-10}	1.0×10^{-7}
(2, 1)	8.8×10^{-8}	3.5×10^{-11}	1.2×10^{-7}	-	7.5×10^{-8}
(1, 0) & (1, 1)	3.8×10^{-7}	1.4×10^{-9}	2.1×10^{-7}	1.9×10^{-9}	3.2×10^{-7}
All above	5.3×10^{-7}	1.6×10^{-9}	3.3×10^{-7}	2.4×10^{-9}	4.9×10^{-7}

^a Due to the symmetry, some modes don't contribute any variation in $\Delta\theta$ and ΔL

Bibliography

- [1] N. Maskelyne, “A proposal for measuring the attraction of some hill in this kingdom by astronomical observations”, *Philosophical Transactions of the Royal Society of London* **65**, 495–499 (1775) 10.1098/rstl.1775.0049.
- [2] R. D. Davies, “A Commemoration of Maskelyne at Schiehallion”, *Quarterly Journal of the Royal Astronomical Society* **26**, 289–294 (1985).
- [3] T. Krisnanda, G. Y. Tham, M. Paternostro, and T. Paterek, “Observable quantum entanglement due to gravity”, *npj Quantum Information* **6**, 10.1038/s41534-020-0243-y (2019) 10.1038/s41534-020-0243-y, arXiv:1906.08808.
- [4] H. Chevalier, A. J. Paige, and M. S. Kim, “Witnessing the nonclassical nature of gravity in the presence of unknown interactions”, *Physical Review A* **102**, 022428 (2020) 10.1103/physreva.102.022428, arXiv:2005.13922.
- [5] J. S. Pedernales, G. W. Morley, and M. B. Plenio, “Motional Dynamical Decoupling for Matter-Wave Interferometry”, *Phys. Rev. Lett.* **125**, 023602 (2019) 10.1103/physrevlett.125.023602, arXiv:1906.00835.
- [6] S. Bose, A. Mazumdar, G. W. Morley, H. Ulbricht, M. Toroš, M. Paternostro, A. Geraci, P. Barker, M. S. Kim, and G. Milburn, “A Spin Entanglement Witness for Quantum Gravity”, *Phys. Rev. Lett.* **119**, 240401 (2017) 10.1103/physrevlett.119.240401, arXiv:1707.06050.
- [7] L. Lami, J. S. Pedernales, and M. B. Plenio, “Testing the quantum nature of gravity without entanglement”, *Phys. Rev. X* **14**, 021022 (2023) 10.1103/physrevx.14.021022, arXiv:2302.03075.
- [8] R. Horodecki, P. Horodecki, M. Horodecki, and K. Horodecki, “Quantum entanglement”, *Rev. Mod. Phys.* **81**, 865–942 (2007) 10.1103/revmodphys.81.865, arXiv:quant-ph/0702225.
- [9] M. B. Plenio and S. Virmani, “An introduction to entanglement measures”, *Quantum Information & Computation* **7**, 1–51 (2005), arXiv:quant-ph/0504163.
- [10] J. S. Pedernales and M. B. Plenio, “On the origin of force sensitivity in tests of quantum gravity with delocalised mechanical systems”, *Contemporary Physics* **64**, 147–163 (2023) 10.1080/00107514.2023.2286074, arXiv:2311.04745.
- [11] D. Carney, P. C. E. Stamp, and J. M. Taylor, “Tabletop experiments for quantum gravity: a user’s manual”, *Classical and Quantum Gravity* **36**, 034001 (2018) 10.1088/1361-6382/aaf9ca, arXiv:1807.11494.

- [12] M. Christodoulou, A. Di Biagio, M. Aspelmeyer, Č. Brukner, C. Rovelli, and R. Howl, “Locally mediated entanglement in linearised quantum gravity”, *Physical Review Letters* **130**, 100202 (2022) 10.1103/physrevlett.130.100202, arXiv:2202.03368.
- [13] Y. Y. Fein, P. Geyer, P. Zwick, F. Kiałka, S. Pedalino, M. Mayor, S. Gerlich, and M. Arndt, “Quantum superposition of molecules beyond 25 kDa”, *Nature Physics* **15**, 1242–1245 (2019) 10.1038/s41567-019-0663-9.
- [14] T. Westphal, H. Hepach, J. Pfaff, and M. Aspelmeyer, “Measurement of Gravitational Coupling between Millimeter-Sized Masses”, *Nature* **591**, 225–228 (2021) 10.1038/s41586-021-03250-7, arXiv:2009.09546.
- [15] H. B. G. Casimir, “On the attraction between two perfectly conducting plates”, *Proc. Kon. Ned. Akad. Wet.* **51**, 793 (1948).
- [16] H. B. G. Casimir and D. Polder, “The Influence of Retardation on the London-van der Waals Forces”, *Physical Review* **73**, 360–372 (1948) 10.1103/physrev.73.360.
- [17] L. Gurvits, “Classical deterministic complexity of Edmonds’ problem and Quantum Entanglement”, in *Proceedings of the thirty-fifth annual acm symposium on theory of computing*, Vol. 4, STOC03 (June 2003), pages 10–19, 10.1145/780542.780545, arXiv:quant-ph/0303055.
- [18] G. Vidal and R. F. Werner, “A computable measure of entanglement”, *Phys. Rev. A* **65**, 032314 (2001) 10.1103/physreva.65.032314, arXiv:quant-ph/0102117.
- [19] M. Plenio, “Logarithmic negativity: a full entanglement monotone that is not convex.”, *Physical Review Letters* **95**, 090503 (2005) 10.1103/PhysRevLett.95.090503, arXiv:quant-ph/0505071.
- [20] T. W. van de Kamp, R. J. Marshman, S. Bose, and A. Mazumdar, “Quantum Gravity Witness via Entanglement of Masses: Casimir Screening”, *Phys. Rev. A* **102**, 062807 (2020) 10.1103/physreva.102.062807, arXiv:2006.06931.
- [21] T. Emig, N. Graham, R. L. Jaffe, and M. Kardar, “Casimir forces between arbitrary compact objects”, *Phys. Rev. Lett.* **99**, 170403 (2007) 10.1103/physrevlett.99.170403, arXiv:0707.1862.
- [22] F. London, “Zur Theorie und Systematik der Molekularkräfte”, *Zeitschrift für Physik* **63**, 245–279 (1930) 10.1007/bf01421741.
- [23] M. Bordag, U. Mohideen, and V. M. Mostepanenko, “New developments in the Casimir effect”, *Physics Reports* **353**, 1–205 (2001) 10.1016/s0370-1573(01)00015-1, arXiv:quant-ph/0106045 [quant-ph].
- [24] G. L. Klimchitskaya, U. Mohideen, and V. M. Mostepanenko, “The Casimir force between real materials: Experiment and theory”, *Reviews of Modern Physics* **81**, 1827–1885 (2009) 10.1103/revmodphys.81.1827, arXiv:0902.4022.

- [25] S. K. Lamoreaux, “The Casimir force: background, experiments, and applications”, Reports on Progress in Physics **68**, 201–236 (2004) 10.1088/0034-4885/68/1/r04.
- [26] M. Bordag, “Proceedings of the Fourth Workshop on Quantum Field Theory under the Influence of External Conditions”, in The Casimir Effect 50 Years Later (June 1999), pages 1–410, 10.1142/9789814527576.
- [27] L. H. Ford, “Casimir Force between a Dielectric Sphere and a Wall: A Model for Amplification of Vacuum Fluctuations”, Phys. Rev. A **58**, 4279–4286 (1998) 10.1103/physreva.58.4279, arXiv:quant-ph/9804055.
- [28] E. M. Lifshitz, “The theory of molecular attractive forces between solids”, Sov. Phys. JETP **2**, 73–83 (1956) 10.1016/b978-0-08-036364-6.50031-4.
- [29] M. Hartmann, “Casimir effect in the plane-sphere geometry: Beyond the proximity force approximation”, PhD thesis (Universität Augsburg, July 2018).
- [30] T. Emig, “Fluctuation induced quantum interactions between compact objects and a plane mirror”, Journal of Statistical Mechanics: Theory and Experiment **2008**, P04007 (2007) 10.1088/1742-5468/2008/04/p04007, arXiv:0712.2199.
- [31] A. Bulgac, P. Magierski, and A. Wirzba, “Scalar Casimir effect between Dirichlet spheres or a plate and a sphere”, Physical Review D **73**, 025007 (2006) 10.1103/physrevd.73.025007.
- [32] I. G. Pirozhenko and M. Bordag, “On the Casimir repulsion in sphere-plate geometry”, Physical Review D **87**, 085031 (2013) 10.1103/physrevd.87.085031, arXiv:1302.5290.
- [33] M. Aspelmeyer, *Quantum sources of gravity: the next frontier of macroscopic quantum physics*, <https://www.youtube.com/watch?v=0AVDrVY-rTw>, Timestamp: 51:00, May 2024.
- [34] A. D. O’Connell, M. Hofheinz, M. Ansmann, R. C. Bialczak, M. Lenander, E. Lucero, M. Neeley, D. Sank, H. Wang, M. Weides, J. Wenner, J. M. Martinis, and A. N. Cleland, “Quantum ground state and single-phonon control of a mechanical resonator”, Nature **464**, 697–703 (2010) 10.1038/nature08967.
- [35] K. C. Lee, M. R. Sprague, B. J. Sussman, J. Nunn, N. K. Langford, X.-M. Jin, T. Champion, P. Michelberger, K. F. Reim, D. England, D. Jaksch, and I. A. Walmsley, “Entangling Macroscopic Diamonds at Room Temperature”, Science **334**, 1253–1256 (2011) 10.1126/science.1211914.
- [36] M. Bild, M. Fadel, Y. Yang, U. von Lüpke, P. Martin, A. Bruno, and Y. Chu, “Schrödinger cat states of a 16-microgram mechanical oscillator”, Science **380**, 274–278 (2022) 10.1126/science.adf7553, arXiv:2211.00449.
- [37] D. Grass, J. Fesel, S. G. Hofer, N. Kiesel, and M. Aspelmeyer, “Optical trapping and control of nanoparticles inside evacuated hollow core photonic crystal fibers”, Applied Physics Letters **108**, 10.1063/1.4953025 (2016) 10.1063/1.4953025, arXiv:1603.09393.

- [38] B. R. Slezak, C. W. Lewandowski, J.-F. Hsu, and B. D’Urso, “Cooling the motion of a silica microsphere in a magneto-gravitational trap in ultra-high vacuum”, *New Journal of Physics* **20**, 063028 (2018) 10.1088/1367-2630/aacac1, arXiv:1802.03424 [quant-ph].
- [39] C. Gonzalez-Ballester, M. Aspelmeyer, L. Novotny, R. Quidant, and O. Romero-Isart, “Levitodynamics: levitation and control of microscopic objects in vacuum”, *Science* **374**, 10.1126/science.abg3027 (2021) 10.1126/science.abg3027, arXiv:2111.05215.
- [40] W. P. Schleich, “Waves à la WKB”, in *Quantum Optics in Phase Space* (John Wiley & Sons, Ltd, Berlin, Feb. 2001) Chap. 5, pages 153–169.
- [41] G. A. E. Vandenbosch, “The basic concepts determining electromagnetic shielding”, *American Journal of Physics* **90**, 672–681 (2022) 10.1119/5.0087295.
- [42] R. Berman, D. K. C. Macdonald, and F. E. Simon, “The thermal and electrical conductivity of copper at low temperatures”, *Proceedings of the Royal Society of London. Series A. Mathematical and Physical Sciences* **211**, 122–128 (1952) 10.1098/rspa.1952.0029.
- [43] R. Gross and A. Marx, *Festkörperphysik*, 3., akt. Aufl, De Gruyter Studium (De Gruyter, Berlin, 2018), 11066 pages.
- [44] J. Dutka, “On the Early History of Bessel Functions”, *Archive for History of Exact Sciences* **49**, 105–134 (1995).
- [45] S. S. Rao, *Vibration of Continuous Systems*, 2nd Edition (Wiley, Jan. 2019), 10.1002/9781119424284.
- [46] M. A. Nielsen and I. L. Chuang, *Quantum computation and quantum information*, 10th anniversary ed. (Cambridge University Press, Cambridge, 2010), 1676 pages.
- [47] D. J. Griffiths, *Elektrodynamik, Eine Einführung*, edited by U. Schollwöck, 4th edition (Pearson, Hallbergmoos, 2018), 1711 pages.
- [48] J. S. Pedernales, K. Streltsov, and M. B. Plenio, “Enhancing Gravitational Interaction between Quantum Systems by a Massive Mediator”, *Physical Review Letters* **128**, 110401 (2021) 10.1103/physrevlett.128.110401, arXiv:2104.14524.
- [49] S. Blanes, F. Casas, J. A. Oteo, and J. Ros, “The Magnus expansion and some of its applications”, *Physics Reports* **470**, 151–238 (2008) 10.1016/j.physrep.2008.11.001, arXiv:0810.5488 [math-ph].

A TITLE TO BE DONE

A.1 Evolution under a gravitational Hamiltonian

In this section the time evolution of a system under Hamiltonian eq. (2.3) is calculated a) using the gravitational interaction \hat{H}_G as a perturbation b) using an exact time evolution of coherent states.

A.1.1 Using time dependent perturbation theory

A general biparty Fock state $|\psi_0\rangle = |kl\rangle$ with $k, l \in \mathbb{N}_0$ can be evolved in time under a Hamiltonian eq. (2.3) treating the gravitational interaction $H_G = -\hbar g(\hat{a}_1\hat{a}_2^\dagger + \hat{a}_1^\dagger\hat{a}_2)$ as a perturbation. The resulting state $|\psi(t)\rangle$ after some time t is in the most general form given as

$$|\psi(t)\rangle = \sum_{i,j \geq 0} c_{i,j}(t) |i, j\rangle \quad (\text{A.1})$$

where the coefficients $c_{i,j}(t)$ are given by first order perturbation theory as

$$c_{i,j}(t) = c_{i,j}(t=0) - \frac{i}{\hbar} \int_0^t dt' \langle ij | \hat{H}_G | kl \rangle e^{-i(E_{kl} - E_{ij})t'/\hbar}. \quad (\text{A.2})$$

The exponent is given by the energy of the appropriate Fock states $E_{kl} - E_{ij} = \hbar\omega(k + l - (i + j))$ and the matrix element in the integrand can be calculated to

$$\langle ij | \hat{H}_G | kl \rangle = \begin{cases} -\hbar g & \text{if } i = k \pm 1 \text{ and } j = l \mp 1 \\ 0 & \text{otherwise} \end{cases}. \quad (\text{A.3})$$

The coefficients for $t = 0$ are trivially given from the initial state as

$$c_{i,j}(t=0) = \begin{cases} 1 & \text{for } i, j = k, l \\ 0 & \text{otherwise} \end{cases}. \quad (\text{A.4})$$

For the non-zero states the energies in the exponent equate to zero and the evolved state is given by (up to a normalization)

$$|\psi(t)\rangle = |kl\rangle - igt |k-1, l+1\rangle - igt |k+1, l-1\rangle + \mathcal{O}(g^2). \quad (\text{A.5})$$

The result eq. (2.5) is represented by eq. (A.5) for the case of $k = 1$ and $l = 0$.

A.1.2 Using an exact time evolution

The Hamiltonian eq. (2.3) can be rewritten using symmetric and antisymmetric normal modes

$$\hat{a}_{\pm} = \frac{1}{\sqrt{2}}(\hat{a}_1 \pm \hat{a}_2) \quad (\text{A.6})$$

in the form of

$$\hat{H} = \hbar\omega_+ \hat{a}_+^\dagger \hat{a}_+ + \hbar\omega_- \hat{a}_-^\dagger \hat{a}_-, \quad \omega_{\pm} = \omega \pm (-g) \quad (\text{A.7})$$

The initial state consisting of two coherent oscillator states is in the new modes given by

$$|\psi(t)\rangle = |\alpha\rangle_1 |\beta\rangle_2 = \left| \frac{1}{\sqrt{2}}(\alpha + \beta) \right\rangle_+ \left| \frac{1}{\sqrt{2}}(\alpha - \beta) \right\rangle_- \quad (\text{A.8})$$

A general coherent state $|\gamma\rangle$ evolves in time under an Hamiltonian $\hat{H} = \hbar\omega \hat{a}^\dagger \hat{a}$ like $|\gamma(t)\rangle = |e^{-i\omega t}\gamma\rangle$ which can be used to evolve the state in eq. (A.8):

$$|\psi(t)\rangle = \left| \frac{1}{\sqrt{2}}e^{-i\omega_+ t}(\alpha + \beta) \right\rangle_+ \left| \frac{1}{\sqrt{2}}e^{-i\omega_- t}(\alpha - \beta) \right\rangle_- \quad (\text{A.9})$$

$$= |e^{-i\omega t}(\alpha \cos gt - \beta \sin gt)\rangle_1 |e^{-i\omega t}(-\alpha \sin gt + \beta \cos gt)\rangle_2, \quad (\text{A.10})$$

where in the last line the back-transformation from the \pm -modes (A.8) was used.

A.2 Exemplary calculation of E_N

In this section, the logarithmic negativity E_N eq. (2.21) is exemplary calculated for the state eq. (2.13). The density matrix of this system is given by

$$\rho(t) = |\psi(t)\rangle\langle\psi(t)| = \frac{1}{4} \begin{pmatrix} 1 & e^{i\Delta\phi} & e^{i\Delta\phi} & 1 \\ e^{-i\Delta\phi} & 1 & 1 & e^{-i\Delta\phi} \\ e^{-i\Delta\phi} & 1 & 1 & e^{-i\Delta\phi} \\ 1 & e^{i\Delta\phi} & e^{i\Delta\phi} & 1 \end{pmatrix}. \quad (\text{A.11})$$

Consequently, the partially transposed density ρ^{Γ_B} is given by

$$\rho^{\Gamma_B}(t) = \frac{1}{4} \begin{pmatrix} 1 & e^{-i\Delta\phi} & e^{i\Delta\phi} & 1 \\ e^{i\Delta\phi} & 1 & 1 & e^{-i\Delta\phi} \\ e^{-i\Delta\phi} & 1 & 1 & e^{i\Delta\phi} \\ 1 & e^{i\Delta\phi} & e^{-i\Delta\phi} & 1 \end{pmatrix}. \quad (\text{A.12})$$

The eigenvalues were calculated using `Mathematica` and equate to

$$\left\{ \sin^2\left(\frac{\Delta\phi}{2}\right), \cos^2\left(\frac{\Delta\phi}{2}\right), \frac{\sin \Delta\phi}{2}, -\frac{\sin \Delta\phi}{2} \right\}$$

According to lemma 2.1, $\|\rho^{\Gamma_B}\|_1$ is given by the sum of the absolute eigenvalues, which is equal to $1 + |\sin \Delta\phi|$. The negativity as the absolute sum of all negative eigenvalues (demonstrated in proposition 2.3) equates to $\mathcal{N} = |\sin \Delta\phi|/2$. Both methods result in a logarithmic negativity of $E_N = \log_2(1 + |\sin \Delta\phi|)$.

B Casimir interactions

B.1 Polarizability of a dielectric sphere

The polarizability α is defined via

$$\mathbf{E}_\infty \alpha = \mathbf{p}, \quad (\text{B.1})$$

where \mathbf{p} is the induced dipole moment and \mathbf{E}_∞ is the external electric field that induces the dipole moment. For a linear and uniform dielectric, it is given as $\mathbf{p} = \mathcal{V} \varepsilon_0 (\varepsilon_r - 1) \mathbf{E}_\text{in}$ [47, p. 220-226]. Here, \mathcal{V} is the volume of the object and \mathbf{E}_in is the electric field inside the dielectric. The electrostatic boundary conditions for the problem are given by

$$V_\text{in}|_{r=R} = V_\text{out}|_{r=R} \quad \text{and} \quad \varepsilon_r \varepsilon_0 \frac{\partial V_\text{in}}{\partial r} \Big|_{r=R} = \varepsilon_0 \frac{\partial V_\text{out}}{\partial r} \Big|_{r=R} \quad (\text{B.2})$$

and the electric potential outside of the sphere at $r \rightarrow \infty$ should be equal to the external dipole-inducing field $V_\text{out}|_{r \rightarrow \infty} = -\mathbf{E}_\infty \cdot \mathbf{r} = -E_\infty r \cos \theta$. The electric potential inside and outside the sphere can be calculated using the spherical decomposition of the general electric potential $V \propto 1/|\mathbf{r} - \mathbf{r}'|$ into Legendre Polynomials P_l [47, p. 188-190]:

$$V_\text{in}(r, \theta) = -E_\infty r \cos \theta + \sum_{l=0}^{\infty} A_l r^l P_l(\cos \theta), \quad (\text{B.3})$$

$$V_\text{out}(r, \theta) = -E_\infty r \cos \theta + \sum_{l=0}^{\infty} \frac{B_l}{r^{l+1}} P_l(\cos \theta). \quad (\text{B.4})$$

Applying both boundary conditions, it follows that [47, p. 249-251]

$$\begin{cases} A_l = B_l = 0 & \text{for } l \neq 1, \\ A_1 = -\frac{3}{\varepsilon_r + 2} E_\infty, \quad B_1 = \frac{\varepsilon_r - 1}{\varepsilon_r + 2} R^3 E_\infty \end{cases} \quad (\text{B.5})$$

and the resulting homogenous electric field $\mathbf{E}_\text{in} = -\nabla V_\text{in}$ inside the sphere is given as

$$\mathbf{E}_\text{in} = \frac{3}{\varepsilon_r + 2} \mathbf{E}_\infty. \quad (\text{B.6})$$

The field is shown on the right in fig. B.1. The polarizability α of the sphere can be now be determined to

$$\alpha_\text{sphere} = 4\pi \varepsilon_0 R^3 \left(\frac{\varepsilon_r - 1}{\varepsilon_r + 2} \right). \quad (\text{B.7})$$

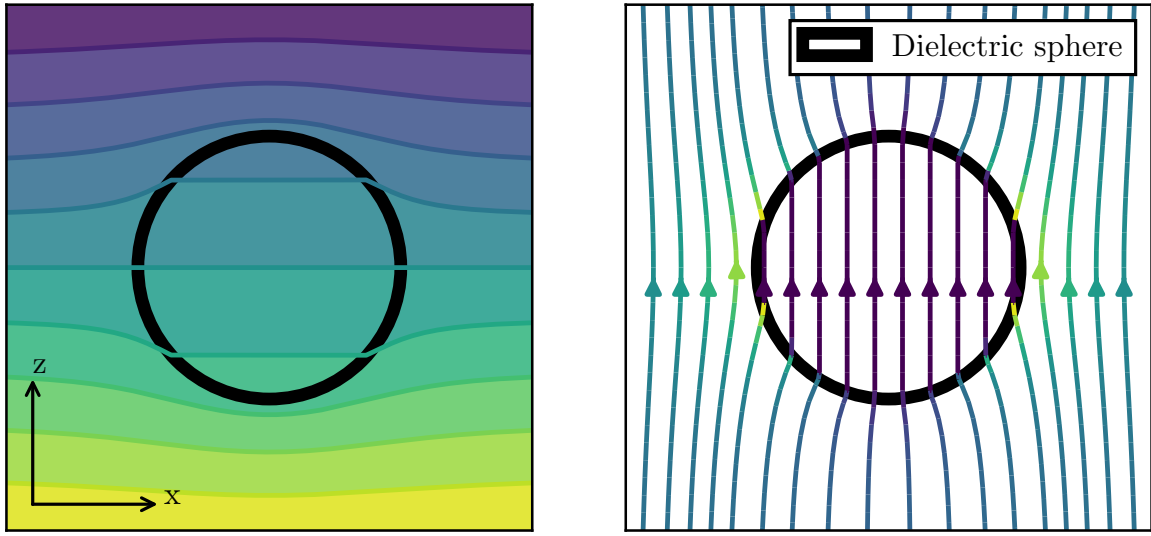


Figure B.1: **left:** Electric potential V of a dielectric sphere in a external electric field $\mathbf{E}_\infty \parallel \mathbf{e}_z$. **right:** The corresponding electric field lines inside and outside the dielectric sphere.

C The shield and its consequences

C.1 Blocking of the shield

Assume two spheres A and B with charge q_A and q_B separated by a distance $2L$ on the x -axis. A circular shield is placed perfectly in the center of the spheres orthogonal to the direct connection between them. The magnitude of the field at a distance z in the direction \mathbf{e}_x from this connection line is given by

$$E_x(z) = \frac{L(q_A - q_B)}{4\pi\epsilon_0(L^2 + z^2)^{3/2}} \quad (\text{C.1})$$

The total flux the circular shield with radius r_s is given by

$$\Phi = \int_0^{r_s} dz \int_0^{2\pi} z d\varphi E_x(z) = \frac{(q_A - q_B)}{2\epsilon_0} \left[1 - \frac{L}{\sqrt{L^2 + r_s^2}} \right]. \quad (\text{C.2})$$

Comparing the total flux for $r_s \rightarrow \infty$ with the flux through the shield, one can arrive at the charge-independent **effectiveness** η of the shield as

$$\eta = \frac{\Phi}{\Phi_\infty} = 1 - \frac{L}{\sqrt{L^2 + r_s^2}} \quad (\text{C.3})$$

and thus a shield with radius

$$r_s = L \sqrt{\frac{1 - (1 - \eta)^2}{(1 - \eta)^2}} \quad (\text{C.4})$$

will block a fraction η of the total field.

C.2 Thermal harmonic oscillator

The amplitude z of a single vibrational shield-mode (k, l) with frequency $\omega_{kl} \equiv \omega$ behaves like a quantum harmonic oscillator. The average amplitude $\langle z \rangle_n = 0$. The variance $(\Delta z)^2 = \langle z^2 \rangle - \langle z \rangle^2$ however is given by

$$(\Delta z)_n^2 = \langle z^2 \rangle_n = \frac{\hbar}{2m\omega} (1 + 2n). \quad (\text{C.5})$$

At a temperature T , the occupation of the modes is described by the boltzmann distribution:

$$\langle z^2 \rangle_T = \sum_{n=0}^{\infty} \frac{1}{Z} e^{-\beta E_n} \langle z^2 \rangle_n, \quad (\text{C.6})$$

where $\beta = 1/k_B T$, $E_n = \hbar\omega(n + 1/2)$ is the energy of mode n and

$$Z = \sum_{n=0}^{\infty} e^{-\beta E_n} = \frac{e^{-\beta \frac{\hbar\omega}{2}}}{1 - e^{-\beta \hbar\omega}} \quad (\text{C.7})$$

is the partition function. Using known series, the expression eq. (C.6) can be evaluated to

$$(\Delta z)_T^2 = \langle z^2 \rangle_T = \frac{\hbar}{2m\omega} \sum_{n=0}^{\infty} \frac{1}{Z} [e^{-\beta E_n} + 2ne^{-\beta E_n}] \quad (\text{C.8})$$

$$= \frac{\hbar}{2m\omega} \left[1 + \frac{2}{Z} \sum_{n=0}^{\infty} ne^{-\beta E_n} \right] \quad (\text{C.9})$$

$$= \frac{\hbar}{2m\omega} \left[1 + \frac{2e^{-\beta \hbar\omega}}{1 - e^{-\beta \hbar\omega}} \right] = \frac{\hbar}{2m\omega} \coth\left(\frac{\hbar\omega}{2k_B T}\right) \quad (\text{C.10})$$

D Calculations

The series expansions of the Casimir terms in the PFA $1/(\mathcal{L}_{A(B)}^i)^2$ from eq. (4.4) are given by:

$$\begin{aligned} \frac{1}{(\mathcal{L}_{A(B)}^i)^2} &\approx \frac{4}{(d-2L+2R)^2} \pm \frac{8\Delta x_{A(B)} \sin \delta}{(d-2L+2R)^3} \pm \theta_{A(B)} \left(\frac{8\Delta x_{A(B)} \cos \delta}{(d-2L+2R)^3} \right) \\ &+ L_{A(B)} \left(\frac{16}{(d-2L+2R)^3} \pm \frac{48\Delta x_{A(B)} \sin \delta}{(d-2L+2R)^4} \right) \pm \theta_{A(B)} L_{A(B)} \frac{48\Delta x_{A(B)} \cos \delta}{(d-2L+2R)^4} \quad (\text{D.1}) \end{aligned}$$

where again the abbreviation $\delta = \alpha, \beta$ was used and the \pm terms align to the corresponding notation in eq. (4.4). The series expansion for the gravitational terms $1/L^{ij}$ with $i, j = 1, 2$ from eq. (4.6) is given by

$$\begin{aligned} \frac{1}{L^{ij}} &= \frac{1}{2L} \pm \frac{\Delta x_B \sin \beta - \Delta x_A \sin \alpha}{8L^2} \mp \theta_A \frac{\Delta x_A \cos \alpha}{8L^2} \pm \theta_B \frac{\Delta x_B \cos \beta}{8L^2} \\ &+ L_A \left(-\frac{1}{4L^2} \pm \frac{\Delta x_A \sin \alpha - \Delta x_B \sin \beta}{8L^3} \right) + L_B \left(-\frac{1}{4L^2} \pm \frac{\Delta x_A \sin \alpha - \Delta x_B \sin \beta}{8L^3} \right) \\ &\pm L_A \theta_A \frac{\Delta x_A \cos \alpha}{8L^3} \mp L_A \theta_B \frac{\Delta x_B \cos \beta}{8L^3} \pm L_B \theta_A \frac{\Delta x_A \cos \alpha}{8L^3} \mp L_B \theta_B \frac{\Delta x_B \cos \beta}{8L^3} \\ &+ L_A L_B \left(\frac{2}{4L^3} \pm \frac{3\Delta x_B \sin \beta - 3\Delta x_A \sin \alpha}{16L^4} \right) \\ &\mp L_A L_B \theta_A \frac{3\Delta x_A \cos \alpha}{16L^4} \pm L_A L_B \theta_B \frac{3\Delta x_B \cos \beta}{16L^4} \quad (\text{D.2}) \end{aligned}$$

The resulting average over $\theta_{A(B)}$ and $L_{A(B)}$ can be computed by

$$\int_{-\infty}^{\infty} d\theta_A d\theta_B dL_A dL_B p(\theta_A) p(\theta_B) p(L_A) p(L_B) e^{i\phi} \quad (\text{D.3})$$

where $p(\cdot)$ is a gaussian probability distribution in the form of

$$p(x) = \frac{1}{\sqrt{2\pi}\Delta x} e^{-\frac{x^2}{2(\Delta x)^2}} \quad (\text{D.4})$$

and ϕ is, as seen in the expansions above, linear in θ_i and L_i with occasional mixed terms. These mixed terms (here denoted by $\Delta A, \Delta B$ for either $\Delta\theta$ or ΔL) can be neglected in first order because in the final result, they appear in the form of

$$\sim \exp \left\{ -\frac{a^2(\Delta A)^2}{2b^2(\Delta A)^2(\Delta B)^2 + 2} \right\} \rightarrow 1 \quad (\text{D.5})$$

D Calculations

which tends to one for small variations $\Delta A, \Delta B \ll 1$ (a, b are constants). Each averaged element of the density matrix can therefore be analytically calculated using

$$\prod_{\Delta A = \{\Delta \theta_{A(B)}, \Delta L_{A(B)}\}} \int_{-\infty}^{\infty} dA \frac{1}{\sqrt{2\pi} \Delta A} e^{-\frac{A^2}{2(\Delta A)^2}} e^{i\phi_1 A} e^{i\phi_2} = \prod_{\Delta A} e^{-\frac{\phi^2(\Delta A)^2}{2}} e^{i\phi_2} \quad (\text{D.6})$$

where again ϕ_1 is the lengthy linearized phase proportional to the series expansions above *and proportional to t* and ϕ_2 is again the lengthy part of the phase independent of the integration parameter A .

As an example, the value of the element $\langle \rho_{12} \rangle$ is given: During time evolution, this element corresponding to $|\psi_A^1 \psi_B^1\rangle \langle \psi_A^1 \psi_B^1|$ picks up the phase (notation from section 4.1)

$$\phi = \phi_{\text{A,Casimir}}^1 + \phi_{\text{B,Casimir}}^1 - \phi_{\text{A,Casimir}}^1 - \phi_{\text{B,Casimir}}^2 + \phi_{\text{Gravity}}^{11} - \phi_{\text{Gravity}}^{12}. \quad (\text{D.7})$$

According to (D.3) and (D.6), the average density matrix element can be calculated analytically yielding

$$\langle \rho_{12} \rangle \approx \exp \left\{ i \left(-\phi_{\text{Casimir}} \frac{16\Delta x_B \sin \beta}{(d-2L+2R)^3} + \phi_{\text{Gravity}} \frac{\Delta x_B \sin \beta}{4L^2} \right) t \right\} \quad (\text{D.8})$$

$$\exp \left\{ - \left(\frac{16\Delta x_B \cos \beta}{(d-2L+2R)^3} \phi_{\text{Casimir}} - \frac{\Delta x_B \cos \beta}{4L^2} \phi_{\text{Gravity}} \right)^2 \frac{(\Delta \theta_B)^2}{2} t^2 \right\} \quad (\text{D.9})$$

$$\exp \left\{ - \left(\frac{\Delta x_B \sin \beta}{4L^3} \phi_{\text{Gravity}} \right)^2 \frac{(\Delta L_A)^2}{2} t^2 \right\} \quad (\text{D.10})$$

$$\exp \left\{ - \left(\frac{96\Delta x_B \sin \beta}{(d-2L+2R)^4} \phi_{\text{Casimir}} + \frac{\Delta x_B \sin \beta}{4L^3} \phi_{\text{Gravity}} \right)^2 \frac{(\Delta L_B)^2}{2} t^2 \right\} \quad (\text{D.11})$$

where

$$\phi_{\text{Casimir}} = \frac{c\pi^3}{720} \left(\frac{\varepsilon_r - 1}{\varepsilon_r + 1} \right) \varphi(\varepsilon_r) R \quad \text{and} \quad \phi_{\text{Gravity}} = \frac{GM_A M_B}{\hbar} \quad (\text{D.12})$$

was used. The resulting logarithmic negativity of $\langle \rho \rangle$ was calculated numerically.